Jointly reduced inhibition and excitation underlies circuit-wide changes in cortical processing in Rett syndrome

Abhishek Banerjee[a,1,2], Rajeev V. Rikhye[a,1], Vincent Breton-Provencher[a], Xin Tang[b], Chenchen Li[c], Keji Li[a], Caroline A. Runyan[a], Zhanyan Fu[c], Rudolf Jaenisch[b,3], and Mriganka Sur[a,3]

[a]The Picower Institute for Learning and Memory, Department of Brain and Cognitive Sciences, Massachusetts Institute of Technology, Cambridge, MA 02139; [b]The Whitehead Institute for Biomedical Research, Cambridge, MA 02142; and [c]Broad Institute of MIT and Harvard, Cambridge, MA 02142

Contributed by Rudolf Jaenisch, September 28, 2016 (sent for review June 12, 2016; reviewed by Uta Francke and Peter Kind)

Rett syndrome (RTT) arises from loss-of-function mutations in methyl-CpG binding protein 2 gene (*Mecp2*), but fundamental aspects of its physiological mechanisms are unresolved. Here, by whole-cell recording of synaptic responses in MeCP2 mutant mice in vivo, we show that visually driven excitatory and inhibitory conductances are both reduced in cortical pyramidal neurons. The excitation-to-inhibition (E/I) ratio is increased in amplitude and prolonged in time course. These changes predict circuit-wide reductions in response reliability and selectivity of pyramidal neurons to visual stimuli, as confirmed by two-photon imaging. Targeted recordings reveal that parvalbumin-expressing (PV^+) interneurons in mutant mice have reduced responses. PV-specific MeCP2 deletion alone recapitulates effects of global MeCP2 deletion on cortical circuits, including reduced pyramidal neuron responses and reduced response reliability and selectivity. Furthermore, MeCP2 mutant mice show reduced expression of the cation-chloride cotransporter KCC2 (K^+/Cl^- exporter) and a reduced KCC2/NKCC1 ($Na^+/K^+/Cl^-$ importer) ratio. Perforated patch recordings demonstrate that the reversal potential for GABA is more depolarized in mutant mice, but is restored by application of the NKCC1 inhibitor bumetanide. Treatment with recombinant human insulin-like growth factor-1 restores responses of PV^+ and pyramidal neurons and increases KCC2 expression to normalize the KCC2/NKCC1 ratio. Thus, loss of MeCP2 in the brain alters both excitation and inhibition in brain circuits via multiple mechanisms. Loss of MeCP2 from a specific interneuron subtype contributes crucially to the cell-specific and circuit-wide deficits of RTT. The joint restoration of inhibition and excitation in cortical circuits is pivotal for functionally correcting the disorder.

MeCP2 | E/I balance | parvalbumin neurons | IGF1 | chloride transporters

Synaptic excitation (E) and inhibition (I), along with the neuronal balance of excitation and inhibition (E/I), is key to the function of brain circuits, and is often disrupted in neurodevelopmental disorders, including autism spectrum disorders (ASDs) (1–3). Rett syndrome (RTT) is a severe neurodevelopmental and adult disorder that arises from sporadic loss-of-function mutations in the X-linked (Xq28) methyl-CpG binding protein 2 gene (*Mecp2*) encoding the protein MeCP2 (4–7). MeCP2 is a critical regulator of brain development and adult neural function (8), and arrested brain maturation due to synaptic dysfunction is one of the hallmarks of RTT (3). However, the effects of MeCP2 on excitatory and inhibitory synaptic mechanisms in vivo, and on neuronal and circuit function underlying RTT pathophysiology, are unknown.

MeCP2 is ubiquitously expressed in multiple cell types and subregions of the brain (4, 6, 9), including inhibitory interneurons, and has cell-autonomous as well as non–cell-autonomous effects (10); thus, it has been particularly challenging to identify its role in cell-specific brain circuits. Anatomically diverse inhibitory interneuron subtypes with distinct physiological signatures influence different aspects of neocortical function and behavior (11, 12). Soma-targeting parvalbumin-expressing (PV^+) and dendrite-targeting somatostatin-expressing (SOM^+) interneurons are the two major nonoverlapping populations of interneurons in mice that target cortical pyramidal neurons (13). Inhibition by PV^+ and SOM^+ neurons powerfully influences neuronal responses and circuit computations in visual cortex (14–17). Deletion of MeCP2 from all forebrain GABAergic interneurons recapitulates key aspects of RTT (18), demonstrating that altered inhibitory function is an important facet of RTT pathophysiology. Indeed, a major phenotype of MeCP2 reduction in individuals with RTT and in mouse models is a propensity for seizures (18–20), suggesting a disruption of inhibitory gating leading to hyperexcitable neuronal populations. Resolving the direction and extent of changes in excitation and inhibition in RTT, within intact cortical circuits, requires direct measurement of excitatory and inhibitory conductances in pyramidal neurons, together with examining how MeCP2 deletion affects cortical processing. Furthermore, causal analysis of how inhibition impacts cells and circuits in RTT requires analysis of MeCP2 loss from particular inhibitory neuron subtypes.

Maturation of GABAergic inhibition depends on the developmental regulation of the neuronal cation-chloride cotransporters KCC2 (K^+/Cl^- exporter) and NKCC1 ($Na^+/K^+/Cl^-$ importer)

Significance

Understanding neurophysiological correlates of neurodevelopmental disorders is one of the pressing challenges of neuroscience. By analyzing a mouse model of Rett syndrome (RTT), we show that cortical pyramidal neurons in methyl-CpG binding protein 2 (MeCP2) mutant mice have reduced excitatory as well as inhibitory synaptic drive. Thus, neuronal response reliability and selectivity, features that arise from excitatory/inhibitory processing circuits within cortex, are reduced. MeCP2 deletion crucially regulates inhibition via two complementary mechanisms: reducing responses of parvalbumin-expressing (PV^+) inhibitory neurons and altering the polarity of GABAergic inhibition in pyramidal neurons. Treating mutant mice with recombinant human insulin-like growth factor-1 (rhIGF1) restores GABAergic polarity along with PV^+ and pyramidal neuron responses, thus providing a mechanistic basis of action of rhIGF1 in RTT.

Author contributions: A.B. and M.S. designed research; A.B., R.V.R., V.B.-P., X.T., C.L., K.L., C.A.R., and Z.F. performed research; A.B., R.V.R., V.B.-P., X.T., C.L., R.J., and M.S. analyzed data; A.B., R.V.R., and M.S. wrote the paper; and R.J. supervised X.T.

Reviewers: U.F., Stanford University; and P.K., University of Edinburgh.

The authors declare no conflict of interest.

[1]A.B. and R.V.R. contributed equally to this work.

[2]Present address: Brain Research Institute, University of Zurich, Zurich CH 8057, Switzerland.

[3]To whom correspondence may be addressed. Email: msur@mit.edu or jaenisch@wi.mit.edu.

This article contains supporting information online at www.pnas.org/lookup/suppl/doi:10.1073/pnas.1615330113/-/DCSupplemental.

(21, 22). Increased intracellular chloride concentration and a change in the postsynaptic impact of GABAergic synapses have been demonstrated during development in mouse models of ASD, including fragile-X syndrome (23, 24). Indirect evidence also points to this mechanism affecting RTT: Lower levels of KCC2 relative to NKCC1 have been found by immunoblot analysis of cerebrospinal fluid samples in patients with RTT (25); depolarizing GABAergic synapses in development follow from down-regulation of brain-derived neurotrophic factor (BDNF) (26), which is also an early consequence of MeCP2 deletion in mouse models (27); and insulin-like growth factor-1 (IGF1) treatment, which partially rescues behavioral and synaptic deficits in mutant mouse models of RTT (28, 29), also activates KCC2 expression and restores the inhibitory action of GABAergic synapses in the hippocampus (30). Thus, the diverse effects of MeCP2 loss may include reducing inhibition via changes in GABA-mediated hyperpolarization.

RTT leads to widespread deficits in brain systems and functions, including vision and gaze, that constitute important ways by which subjects with RTT interact with their surroundings (31, 32). RTT is marked by arrested development of visual processing (33), atypical visually evoked cortical responses (34, 35), deficits in visual attention and recognition, and unusual gaze intensity (36). In primary visual cortex (V1), "simple" stimuli, such as oriented gratings, and "complex" stimuli, such as natural scenes, activate local and distributed circuits that lead to well-defined responses from visual cortex neurons (37–41). Importantly, the timing and amplitude of visually driven excitatory and inhibitory conductances powerfully shape the spike responses of V1 neurons, including response reliability, selectivity, and signal-to-noise ratios (40, 42, 43). Analysis of alterations in visual responses and neuronal information processing in MeCP2 mutant mice thus provides both a mechanistic understanding of visual deficits in RTT as well as sensitive assays of changes in synaptic integration and neuronal circuits. Furthermore, visual cortical plasticity is influenced by maturation of excitation and inhibition in cortical circuits (44–47), and the initiation and termination of critical period plasticity in V1 of MeCP2 mutant mice is a sensitive indicator of the level of inhibition in cortical circuits.

Here, by directly measuring visually driven synaptic conductances in V1 pyramidal neurons in vivo, we show that both excitatory and inhibitory conductances are reduced in MeCP2 mutant mice. By deleting MeCP2 only from PV^+ or SOM^+ neurons, we deconstruct the effects of global deletion. PV^+ neurons, which regulate E/I balance in cortical circuits (48), are crucial for recapitulating the key circuit effects of global MeCP2 loss: Animals with PV-specific MeCP2 deletion show reduced PV^+ as well as pyramidal neuron responses, reduced signal-to-noise ratio and response reliability, altered between-neuron signal and noise correlations, and altered ocular dominance (OD) plasticity, comparable to global MeCP2 mutant mice. MeCP2 mutant mice show reduced expression of KCC2, and hence altered KCC2/NKCC1 ratios, and pyramidal neurons have depolarized GABA reversal potentials that are restored by application of the NKCC1 inhibitor bumetanide. Application of IGF1, which improves a range of behavioral and cellular phenotypes in MeCP2 mutant mice (28, 29) and structural, functional, and molecular phenotypes in patient-derived MeCP2-deficient human neurons (49, 50), renormalizes KCC2 expression in mutant mice, and restores PV^+ as well as pyramidal neuron responses. These findings indicate that reduction of both inhibition and excitation, importantly via MeCP2 effects on PV^+ neurons and KCC2, underlies the cortical circuit deficits of RTT, and restoration of inhibition and excitation together may be crucial for ameliorating RTT dysfunction.

Results

Deletion of MeCP2 Decreases Visually Evoked Synaptic Conductances and Visual Responses in Layer 2/3 Pyramidal Neurons. To probe alterations directly in excitation and inhibition in pyramidal neurons after MeCP2 deletion, we used in vivo whole-cell patch-clamp recordings to measure both excitatory (G_e) and inhibitory (G_i) synaptic conductances from putative excitatory layer (L) 2/3 neurons in V1 of mice at postnatal day (P) ∼45 (Fig. 1*A*, *Materials and Methods*, and *SI Materials and Methods*). In voltage-clamp mode, we measured the postsynaptic currents elicited by drifting visual gratings presented at the neuron's preferred orientation (Fig. 1*B*). To isolate visually evoked excitatory postsynaptic currents (EPSCs) and inhibitory postsynaptic currents (IPSCs), we held neurons at the reversal potential for excitatory (−70 mV) and inhibitory (+20 mV) currents, respectively. We analyzed the most reliable responses by averaging synaptic currents during the first 500 ms of stimulus presentation when synaptic responses were largest (Fig. 1*C*). Visually evoked synaptic conductances derived from the EPSC and IPSC traces in age-matched (P45) wild-type (WT) and MeCP2 global null male mice [*Mecp2*$^{-/y}$ or global KO (gKO)] showed that deletion of MeCP2 significantly reduced both total excitatory and inhibitory conductance in superficial layer pyramidal neurons (Fig. 1 *D* and *E*). Measurements of E/I ratio during the onset of the visual response revealed that although the ratio initially increased, inhibition rapidly surpassed excitation in WT mice, whereas in gKO mice, inhibition remained lower than excitation for a prolonged period (Fig. 1*F*). The total E/I ratio in MeCP2 gKO mice tended to be higher compared with WT mice (Fig. 1*G*). Consistent with a reduction in excitatory conductance, cell-attached recordings from putative L2/3 pyramidal neurons in MeCP2 gKO mice showed significantly reduced peak responses at the optimal orientation and reduced orientation selectivity index (OSI) compared with excitatory neurons in WT mice (Fig. 1 *H*–*J*). [The OSIs of WT neurons recorded here were comparable to the OSIs in several other studies in mouse V1 (51), including identified and reconstructed pyramidal neurons (52)]. Similar to gKO mice, mice with excitatory neuron [calmodulin-dependent protein kinase II (CaMKII)]-specific deletion of MeCP2 also showed reduced OSIs (Fig. 1 *H* and *I*) and reduced peak responses at the optimal orientation compared with excitatory neurons in WT littermate controls (Fig. 1*J*). Overall, these results demonstrate that global deletion of MeCP2 reduces and alters the timing of visually evoked excitatory and inhibitory synaptic conductances in V1 pyramidal neurons, along with their peak responses and orientation selectivity. Excitatory neuron (CaMKII)-specific deletion of MeCP2 has a similar effect on peak responses and orientation selectivity, suggesting that MeCP2 effects are manifest through V1 circuits that generate and maintain response specificity and tuning.

MeCP2 Deletion from Inhibitory Interneuron Subtypes Alters Interneuron Responses and Selectivity. Given that MeCP2 affects both excitatory and inhibitory drive to cortical neurons, we asked whether specific subtypes of inhibition were influenced by MeCP2. PV^+ and SOM^+ interneurons provide distinct forms of inhibition to cortical pyramidal neurons (12). We hypothesized that these principal sources of inhibition to pyramidal neurons would be affected by MeCP2 deletion; in turn, deleting MeCP2 from PV^+ or SOM^+ neurons would reveal specific and distinct contributions of these cell types to circuit dysfunction underlying RTT pathophysiology.

To test these hypotheses, we used two-photon–guided cell-attached recordings to measure the stimulus-evoked properties of PV^+ and SOM^+ neurons in MeCP2 gKO mice. We also deleted MeCP2 specifically from either PV^+ or SOM^+ neurons using Cre/loxP recombination [to generate *PV-Mecp2*$^{-/y}$ or PV–cell-specific conditional KO (cKO) and *SOM-Mecp2*$^{-/y}$ or SOM-cKO mice] and measured cell-specific responses (Fig. 2 *A*–*C*, *Materials and Methods*, Fig. S1 *A* and *B*, and *SI Materials and Methods*). The PV locus is turned on late during postnatal development (53, 54), and Cre-dependent deletion of MeCP2 in PV^+ neurons was found to be complete only around P60, with substantial MeCP2 still expressed in these neurons at P30 (Fig. S1*A*). Thus, we restricted our analysis of PV-cKO animals to ages P60 and older. Mice with interneuron-specific deletion of MeCP2

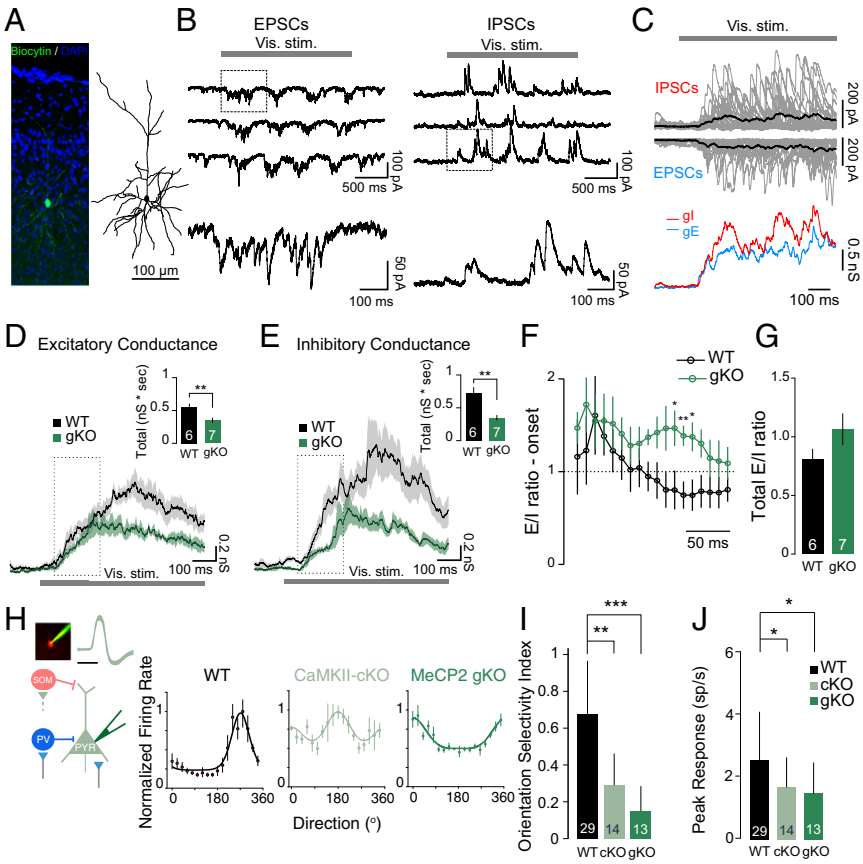

Fig. 1. MeCP2 deletion leads to reduction of visually evoked synaptic conductances and spike responses in pyramidal neurons. (*A*) Confocal image (*Left*) and reconstruction (*Right*) of an L2/3 pyramidal neuron in a WT mouse filled with biocytin during whole-cell in vivo patch-clamp recording in V1. (*B*, *Upper*) Example traces of visually evoked EPSCs and IPSCs at holding potentials of −70 mV (*Left*) and +20 mV (*Right*). Drifting grating stimulation was presented at the neuron's preferred orientation at a temporal frequency of 2 Hz. (*B*, *Bottom*) Traces in the boxed areas are expanded. (*C*, *Top*) Averaged postsynaptic currents in a WT neuron during the first 500 ms after the onset of visual stimuli. Gray traces represent single trials, and black traces represent the average. (*C*, *Bottom*) Corresponding synaptic conductance derived from the voltage-clamp recordings. (*D*) Population-averaged traces of the excitatory conductance for WT (n = 6 neurons from five mice) and MeCP2 gKO (n = 7 neurons from four mice) animals. (*Inset*) Mean ± SEM of the total excitatory conductance. (*E*) Population-averaged traces. (*Inset*) Mean ± SEM of the total inhibitory conductance. (*F*) Timing of E/I ratio after the onset of the visual response as highlighted by the boxes in *D* and *E*. Mean E/I ± SEM ratio for each time point was calculated over 10-ms intervals. (*G*) Summed E/I ratio (0–500 ms poststimulus onset) for WT and gKO cells. (*H*) Orientation-selective responses of pyramidal neurons in WT (n = 29 neurons from 12 mice), gKO (n = 14 neurons from six mice), and CaMKII-cKO (n = 13 neurons from six mice) animals as probed by in vivo two-photon–guided cell-attached recordings (*Left*, *Inset*). (Scale bar: 1 ms.) Mean OSI (*I*) and peak response (*J*) at the preferred orientation of excitatory neurons are shown. sp/s, spikes per second. The number of cells recorded is marked in the histogram bars. All values are expressed as mean ± SEM. $*P < 0.05$, $**P < 0.001$, $***P < 0.0001$; Wilcoxon rank-sum test. Vis. stim., visual stimuli.

showed several key behavioral phenotypes that are observed in gKO mice or in mice with MeCP2 deletion in selective forebrain GABAergic neurons (55).

We found that the OSI was significantly reduced in both MeCP2-deleted PV$^+$ and SOM$^+$ neurons in cKO mice, as well as in the same neurons in gKO mice, compared with control neurons (Fig. 2 *D* and *E*). [The OSIs of PV$^+$ neurons in WT mice reported here (range: 0.11–0.93, mean = 0.48) matched well with the OSIs (range: 0.09–0.87, mean = 0.46) recorded in identified and morphologically reconstructed PV$^+$ neurons in WT mice (52), which found that PV$^+$ neurons with high OSIs (cf. 56, 57) had small somata and dendritic arbors. Other studies have described only broadly tuned inhibitory neurons, particularly with Ca^{2+} imaging (58). The OSIs of SOM$^+$ neurons we recorded in WT mice matched well with the OSIs of SOM$^+$ neurons reported by others (59, 60).] Deleting MeCP2 from PV$^+$ neurons also led to a significant reduction in firing rate at the preferred orientation (Fig. 2*E*). A similar effect, however, was not seen for SOM$^+$ neurons in either the cKO or gKO condition (Fig. 2*F*). Thus, global or cell-specific MeCP2 deletion affects PV$^+$ neurons more severely than SOM$^+$ neurons.

Interneuron-Specific MeCP2 Deletion Leads to Circuit-Wide Deficits in Visual Information Processing. Extracting and encoding salient features of visual stimuli is a core function of neural circuits in V1. Our data thus far suggest that deleting MeCP2 from cortical interneuron subtypes reduces excitatory drive to PV$^+$ and alters the selectivity of PV$^+$ and SOM$^+$ neurons. We were next interested in understanding how this change in interneuron responses influences V1 pyramidal neuron responses and the computations performed by these neurons. To study large populations of putative L2/3 pyramidal neurons in vivo at single-cell resolution, we performed high-speed Ca^{2+} imaging after loading cells with the synthetic calcium indicator dye Oregon green BAPTA-1 (OGB-1) AM (Fig. 3*A*, *Materials and Methods*, and *SI Materials and Methods*). As expected, pyramidal cells in both PV-cKO and SOM-cKO mice responded to full-field sinusoidal drifting gratings with robust Ca^{2+} transients (Fig. 3*B*). We inferred spiking rates from these Ca^{2+} responses using a temporal deconvolution algorithm (61), and used these inferred firing rates to obtain orientation-tuning curves (Fig. 3*C*). Interestingly, both the average firing rate (Fig. 3*D*) and signal-to-noise ratio measured at the preferred orientation (Fig. 3*E*) were reduced in pyramidal neurons in the PV-cKO, SOM-cKO, and

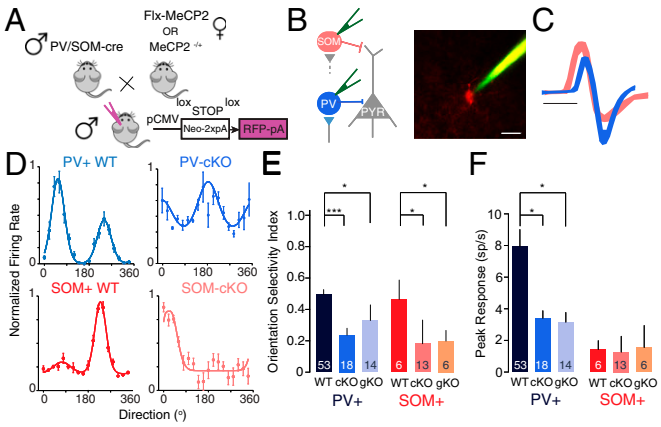

Fig. 2. Deletion of MeCP2 alters response features and selectivity of interneuron subtypes. (*A*) Experimental schematic depicting breeding strategy where homozygous PV-cre and SOM-cre animals were crossed either with floxed (flx)-MeCP2 or *Mecp2*$^{-/+}$ (MeCP2 Het) females to generate conditional cKO and gKO mice. Neo-2xpA, a neomycin STOP cassette with 2 poly-adenylation sites; PCMV, CMV promoter and β-globin intron (52). (*B*) In vivo targeted cell-attached recording from identified MeCP2-deleted PV$^+$ and SOM$^+$ cells. RFP$^+$ cells were targeted under a two-photon microscope with a pipette filled with Alexa 488. PYR, pyramidal cells. (*C*) Spike shapes from PV$^+$ and SOM$^+$ cells showing regular-spiking (SOM, pink) and fast-spiking (PV, blue) neurons. (Scale bar: 1 ms.) (*D*) Example orientation-selective responses of PV$^+$ and SOM$^+$ neurons in cKO animals. Quantification of mean OSI (*E*) and peak response (*F*) of PV$^+$ and SOM$^+$ neurons in cKO and gKO animals are shown. Data are averaged from PV WT (n = 53 neurons from 15 mice), PV-cKO (n = 18 neurons from seven mice), and PV-gKO (n = 14 neurons from five mice) animals and from SOM WT (n = 6 neurons from five mice), SOM-cKO (n = 13 neurons from five mice), and SOM-gKO (n = 6 neurons from three mice) animals. The number of cells recorded is marked in the histogram bars. All values are expressed as mean ± SEM. *P < 0.05, ***P < 0.0001; Wilcoxon rank-sum test.

MeCP2 gKO mice compared with WT and floxed-MeCP2 control mice. Thus, deleting MeCP2 specifically from interneurons causes a reduction in visually evoked activity of pyramidal neurons and a commensurate increase in trial-to-trial variability.

As expected from previous studies in mouse V1, we found a wide range of OSI values in both WT and MeCP2-deficient mice (Fig. 3*F*). Pyramidal cells in PV-cKO and MeCP2 gKO mice had significantly lower OSI values (Fig. 3*G*), but, surprisingly, cells in SOM-cKO mice showed no change in OSI relative to WT or floxed-MeCP2 mice. Thus, even though MeCP2-deleted SOM$^+$ neurons show weak orientation selectivity themselves (Fig. 2*E*), this weak orientation selectivity did not affect the orientation selectivity of their target pyramidal cells. Furthermore, OSI values in MeCP2 gKO mice were only marginally lower than in PV-cKO mice (P = 0.049, Bonferroni-corrected rank-sum test). Given that anesthesia can impede the function of cortical interneurons (42), we repeated these experiments in awake, head-fixed, passively viewing mice (Fig. S2). In these mice, we confirmed our observation that PV-cKO mice also had reduced pyramidal neuron firing rates and orientation selectivity. Thus, deleting MeCP2 from PV$^+$ neurons alone has a strong, deleterious effect on visual responses and orientation selectivity in V1, and the deficits seen in MeCP2 gKO mice can be explained, at least to some extent, by a lack of MeCP2 in PV$^+$ neurons.

To further examine the impact of MeCP2 deletion from PV$^+$ and SOM$^+$ neurons on network-dependent computations, we presented visually complex natural movies instead of simple sinusoidal gratings. Natural movies are broadband in both spatial frequency and orientation, and therefore elicit complex interactions between neurons (62). Neurons in WT mice responded strongly and synchronously to natural movies (Fig. 4*A*). On average, neurons in PV-cKO and MeCP2 gKO mice responded weakly and with greater variability, and hence with a reduced signal-to-noise ratio, compared with neurons in WT and floxed-MeCP2 animals (Fig. 4 *A–D* and Fig. S2 *D* and *E*). We found no significant reduction in average firing rate or signal-to-noise ratio for neurons in SOM-cKO mice.

Natural scenes are represented in V1 with sparse and reliable responses (39, 40). For example, a highly reliable neuron would respond with low variability between trials, and thus would convey similar information for each stimulus repetition. In addition, a sparsely responding neuron is highly selective for a few stimulus features (63). We used these measures to assess how deleting MeCP2 from specific inhibitory neuron subtypes influences cortical coding. We computed response reliability as the average correlation coefficient over all pairwise combinations of trials (*Materials and Methods* and *SI Materials and Methods*). On average, neurons in PV-cKO and MeCP2 gKO mice, but not in SOM-cKO mice, responded unreliably to natural movies (Fig. 4*E* and Fig. S2*G*). At the same time, excitatory neurons in PV-cKO and SOM-cKO mice, as well as in gKO mice, responded to natural movies with significantly less selective responses (Fig. 4*F*), implying a reduction in coding efficacy. Thus, SOM-cKO animals show deficits in stimulus selectivity but can still reliably transmit information, suggesting a subtle deficit in information processing.

To probe these circuit deficits further, we asked how deleting MeCP2 influences the interactions between neurons. Signal correlations between neuronal responses arise from dependencies between neurons sharing similar receptive field properties, and thus provide a measure of similarity in feed-forward input (64). Noise correlations, on the other hand, capture dependencies between neurons that are not locked to the sensory stimulus, and thus are related to shared network properties, including neuronal coupling (65). Deleting MeCP2 from PV$^+$ neurons, but not SOM$^+$ neurons, resulted in a strong reduction in signal correlation (Fig. 4*G*). Signal

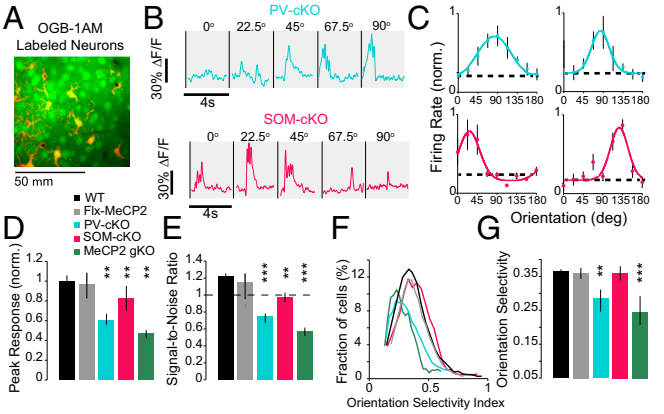

Fig. 3. Deleting MeCP2 results in weak and unselective responses to sinusoidal gratings. (*A*) Example of an OGB1-AM–labeled population of neurons. Neurons were identified by OGB1 expression (green), whereas astrocytes were identified by SR-101 expression (red). Astrocytes were discarded from further analysis (*Materials and Methods*). Representative Ca^{2+} responses (*B*) and orientation tuning curves (*C*) from two neurons from PV-cKO (*Top*) and SOM-cKO (*Bottom*) mice. The Ca^{2+} responses correspond to the leftmost tuning curves in *C*. Error bars represent SEM across 10 repeats of each orientation. deg, degrees; ΔF/F, changes in fluorescence activity. Normalized peak response (*D*) and signal-to-noise ratio (*E*) at the preferred orientation for each of the five experimental conditions are shown. Histogram (*F*) and normalized OSI (*G*) values for the five different experimental conditions are shown. Bar colors denote experimental conditions as labeled in *D*. Data are averaged from WT (327 neurons from six mice), flx-MeCP2 (270 neurons from six mice), PV-cKO (146 neurons from four mice), SOM-cKO (240 neurons from four mice), and MeCP2 gKO (163 neurons from four mice) animals. Error bars denote SEM. *P < 0.05, **P < 0.01, ***P < 0.001; Kruskal–Wallis ANOVA followed by post hoc Bonferroni-corrected rank-sum tests relative to WT.

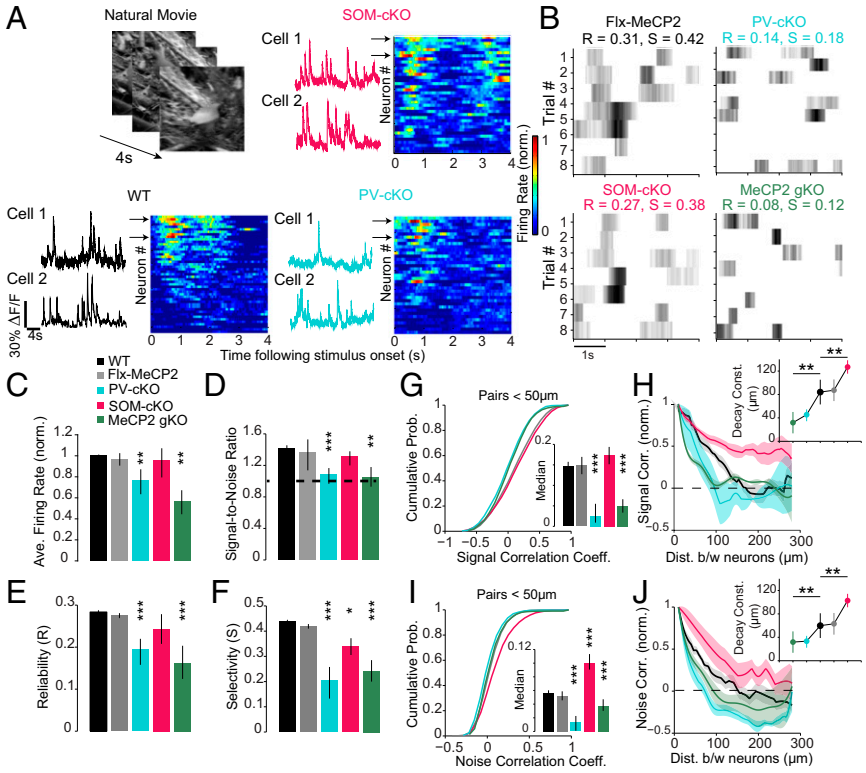

Fig. 4. Impaired processing of complex stimuli in MeCP2-deficient mice. (*A*) Example frames from a natural movie lasting 4 s (*Top Left*). Example Ca^{2+} responses from two simultaneously recorded neurons from WT control (*Bottom Left*), PV-cKO (*Bottom Right*), and SOM-cKO (*Top Right*) mice. The heat maps show the normalized firing rates from simultaneously recorded populations of neurons. (*B*) Example raster plot (trials vs. time) of a representative neuron from flx-MeCP2 control, PV-cKO, SOM-cKO, and MeCP2 gKO mice. The reliability (R) and selectivity (S) values for each neuron are labeled. Mean firing rate (*C*) and signal-to-noise ratio (*D*) of neurons in the five experimental conditions to natural movies are shown. Quantification of reliability (*E*) and selectivity (*F*) for each of the five experimental conditions are shown. (*G*) Cumulative distribution of signal correlation coefficient between pairs of neurons closer than 50 μm apart. Prob., probability. (*Inset*) Bootstrapped estimate of median signal correlation coefficient (Coeff.). Error bars denote the 95% confidence interval of the median. (*H*) Signal correlation coefficient as a function of distance between neurons. The shaded area denotes the 95% confidence interval of the median. (*Inset*) Correlation decay coefficient obtained by fitting single exponentials to the curves in *H*. $^{**}P < 0.01$, Wilcoxon rank-sum test relative to WT control. b/w, between; Const., constant; Dist., distance. (*I* and *J*) Same as *G* and *H*, respectively, but for noise correlation coefficient. Bar colors denote experimental conditions as labeled in *E*. Error bars denote SEM. (*C–F*, *G*, and *I*) $^{*}P < 0.05$, $^{**}P < 0.01$, $^{***}P < 0.001$; Kruskal–Wallis ANOVA followed by post hoc Bonferroni-corrected rank-sum tests relative to WT. Data are averaged from WT (515 neurons from eight mice), flx-MeCP2 (380 neurons from six mice), PV-cKO (146 neurons from four mice), SOM-cKO (240 neurons from four mice), and MeCP2 gKO (163 neurons from four mice) animals.

correlations between neurons persisted over a longer distance in SOM-cKO mice (Fig. 4*H*, *Inset*), consistent with the role of SOM^+ neurons in integrating information over a larger area in L2/3. In contrast, signal correlations decayed more rapidly in PV-cKO and MeCP2 gKO animals compared with WT mice. Noise correlations were also reduced in PV-cKO and MeCP2 gKO animals, but increased in SOM-cKO animals (Fig. 4*I*). Across the imaged population, noise correlations decreased almost exponentially between neurons in all conditions, but persisted over a longer distance in SOM-cKO mice (Fig. 4*J*, *Inset*). Although PV-specific deletion decreased the magnitude and spatial extent of noise correlations, similar to global Mecp2 deletion, and SOM-specific deletion increased noise correlations, the impact of either change was to decrease selectivity (Fig. 4*F*), consistent with the observation that V1 in WT animals is remarkably efficient at coding natural scenes, and any perturbation would alter selectivity (41). Importantly, the deficits in gKO mice were nearly completely recapitulated in PV-cKO mice, indicating that deletion of MeCP2 from PV^+ neurons is sufficient for the circuit-wide deficits of global MeCP2 deletion.

Interneuron-Specific MeCP2 Deletion Prolongs Experience-Dependent Cortical Plasticity. In V1, a change in the ocular dominance index (ODI) is a robust measure of the ability of visual cortex circuits to reorganize in response to changes in eye-specific drive; such reorganization is prominent during the critical period for OD plasticity (66) (Fig. S3*A*). A specific level of inhibition is thought to control the opening of the critical period, whereas increased, mature levels of inhibition reduce or terminate it in adulthood (45, 46). Furthermore, reduction of PV^+ firing can extend the critical period for OD plasticity (67), as can manipulations in adult animals that reduce intracortical inhibition (68, 69). Thus, we hypothesized that adult gKO or PV-cKO mice, which show reduced inhibition in pyramidal neurons and reduced PV^+ responses, would show prolonged OD plasticity in adulthood.

We tested this hypothesis by measuring the ODI in V1 of adult male mice using optical imaging of intrinsic signals (*Materials and Methods* and *SI Materials and Methods*). Eye-specific responses were measured from V1 following short-term (3–4 d) monocular deprivation (MD) of the contralateral eye. MD reduced responses to the deprived eye and shifted the ODI toward the nondeprived eye in WT animals (Fig. S3*B*). This shift, however, was restricted to the critical period of OD plasticity (peaking at P28–30), because no significant change in ODI was seen following MD in adult (P56–60) WT mice (Fig. S3*B*). Similarly, adult floxed-MeCP2 animals (P56–60) also did not show a change in ODI following short-term MD (Fig. S3*C*). Adult MeCP2 gKO male mice were near the end of their life span by P60 (and were too fragile for these experiments); adult female ($Mecp2^{-/+}$) mice, however, showed

OD plasticity at P60 at levels comparable to the levels measured during the critical period (28). Similarly, adult male PV-cKO mice showed a significant shift in ODI (Fig. S3*D*), in contrast to adult WT and floxed-MeCP2 mice. Thus, PV-specific MeCP2 deletion causes deprivation-induced plasticity of visual cortex circuits to extend into adulthood, consistent with a reduction of inhibition in these animals.

Recombinant Human IGF1 Improves Cell-Specific Response Features and Network-Dependent Computations. Recombinant human IGF1 (rhIGF1) has been shown to ameliorate a wide range of deficits in male *Mecp2*$^{-/y}$ null mice as well as female *Mecp2*$^{-/+}$ mice, including organismal and behavioral function, molecular signaling pathways, and excitatory synaptic transmission; rhIGF1 also reverses prolonged cortical plasticity in adult female *Mecp2*$^{-/+}$ mice (28). If a reduction of PV$^+$ neuron responses is critically associated with the circuit-level effects of MeCP2 deletion, rhIGF1 should restore PV$^+$ responses and the circuit-level deficits of information processing by V1 neurons.

We first investigated whether rhIGF1 treatment improves the response features of PV$^+$ neurons in PV-cKO mice. We injected a lox-STOP-lox RFP construct in V1 (compare Fig. 2*A*), followed by daily systemic injections either with saline (control) or rhIGF1 (2.5 mg/kg), following doses (28) shown to be effective for rescuing synaptic and behavioral phenotypes (Fig. 5*A*). The IGF1 receptor is present on both pyramidal and PV$^+$ neurons as revealed by immunohistochemistry (Fig. 5*B*), suggesting that PV$^+$ neurons could respond directly to IGF1 treatment as well as indirectly via recurrent connections from pyramidal neurons. Two-photon–guided cell-attached recordings from PV$^+$ neurons showed approximately a 50% increase in peak firing rate (Fig. 5*C*) and a smaller increase in OSI (Fig. 5*C*). Two-photon Ca^{2+} imaging of OGB-1–labeled pyramidal neurons in PV-cKO mice revealed that rhIGF1 treatment also increased the OSI in response to drifting gratings (Fig. 5*D*), as well as average firing rate, signal-to-noise ratio, and response reliability in response to natural movies (Fig. 5 *E*–*G*). Similarly, pyramidal neurons in MeCP2 gKO mice treated with rhIGF1 (Fig. 5*A*) also showed improvements in these parameters when responding to natural movies, as well as increased OSI comparable to rhIGF1-treated PV-cKO mice when tested with drifting gratings (Fig. 5 *D*–*G*).

These results demonstrate that rhIGF1 treatment enhances responses of PV$^+$ neurons in PV-cKO mice and of pyramidal neurons in both PV-cKO and gKO mice, and, further, that rhIGF1 treatment improves the representation of both simple and complex stimuli by V1 circuits. Thus, deficits caused by MeCP2 deletion in circuits performing sensory computations can be specifically ameliorated by rhIGF1 treatment.

GABAergic Neurotransmission Is Altered in MeCP2 gKO Mice and Rescued by Bumetanide and rhIGF1. Although our whole-cell recordings in MeCP2 gKO mice demonstrated reduced inhibitory conductances in V1 pyramidal neurons, and targeted recordings from PV$^+$ neurons in these mice revealed that they have reduced visual responses, other studies have described increased puncta and perisomatic terminations of PV$^+$ neurons around V1 pyramidal neurons in gKO mice (70, 71), although with no change in other structural and maturational markers of PV$^+$ neurons, such as homeobox protein Otx2 (72) and perineuronal nets (68) (Fig. S4). To reconcile these observations, we hypothesized that the effectiveness of GABA as an inhibitory transmitter may be altered in gKO mice compared with WT animals. The development of GABAergic inhibitory transmission is associated with expression of neuronal cation-chloride cotransporters and an excitatory-to-inhibitory shift in GABA polarity, which indeed is compromised in several mouse models of autism (23); furthermore, early developmental alteration of GABA polarity exerts a long-lasting effect on critical period plasticity in visual cortex (26).

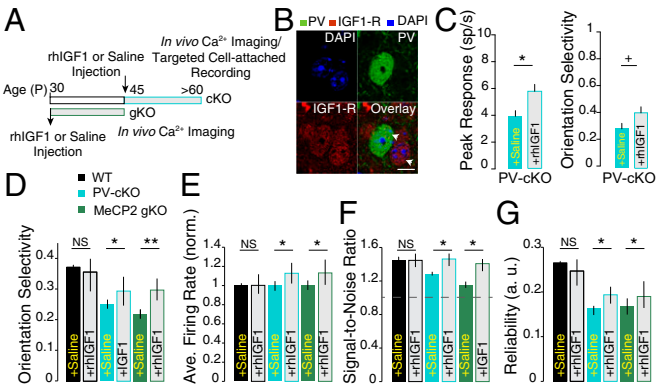

Fig. 5. rhIGF1 treatment restores response rate, selectivity, and reliability in MeCP2-deleted mice. (*A*) Schematic showing timeline of rhIGF1 administration and experiments. MeCP2 gKO animals were treated (by i.p. injection) for 2 wk (starting at P30), and recordings were performed at ∼P45; treatment for PV-cKO animals was started at P45, and Ca^{2+} imaging and electrophysiological recordings were done at ∼P60. Control animals received saline injections. (*B*) Immunohistochemical labeling showing the presence of IGF1 receptor (IGF1-R; red) in PV$^+$ interneurons (green), and excitatory neurons in L2/3 of mouse V1. Arrowheads (white) in the overlay show a PV$^+$ interneuron and a neighboring excitatory neuron, both expressing IGF1-R. (Scale bar: 10 μm.) (*C*) Two-photon–guided cell-attached recording from PV$^+$ cells in saline-treated (control, n = 10 neurons from four mice) and rhIGF1-treated (n = 10 neurons from five mice) animals in response to drifting gratings. Values are normalized to saline controls. (*D*) Ca^{2+} imaging of responses, showing normalized OSI computed from responses to drifting gratings. Normalized mean firing rate (*E*) and signal-to-noise ratio (*F*) in response to natural movies are shown. a.u., arbitrary units. Data are averaged from WT [saline (189 neurons from four mice)], WT [rhIGF1 (157 neurons from four mice)], PV-cKO [saline (294 neurons from four mice)], PV-cKO [rhIGF1 (207 neurons from four mice)], MeCP2 gKO [saline (277 neurons from three mice)], and MeCP2 gKO [rhIGF1 (125 neurons from three mice)] animals. (*G*) Normalized response reliability computed from response to natural movies. All values in *D*–*G* are normalized to saline controls and represented as mean ± SEM. Bar colors denote experimental conditions as labeled in *D*. $^+P = 0.06$, $^*P < 0.05$, $^{**}P < 0.001$; Wilcoxon rank-sum test relative to saline control.

To test the hypothesis, we carried out perforated patch recordings from L2/3 pyramidal neurons in V1 slices from MeCP2 gKO mice and WT littermate controls (Fig. 6*A*), and measured the reversal potential (E_{Cl}^-) for $GABA_A$ receptor-mediated responses, by recording these responses while the membrane voltage was clamped at various holding potentials between –80 mV and +40 mV (Fig. 6 *B*, *i*). Plotting current–voltage relationships (Fig. 6 *B*, *ii*) showed that cells recorded from MeCP2 gKO mice had significantly depolarized GABA reversal potentials compared with cells in WT littermate controls (E_{Cl}^- in gKO mice was, on average, 8 mV more depolarized compared with WT), with no difference in their resting membrane potential (Fig. 6*C*). To test the role of Cl^- cotransporters in GABA polarity directly, we used bumetanide, an NKCC1 antagonist that has previously been shown to decrease internal Cl^- concentration in neurons, making the action of GABA more hyperpolarizing (73). Systemic administration of bumetanide to MeCP2 gKO mice through i.p. injection (for 3–4 d) together with bath application (100 μM) reversed the deficit in E_{Cl}^- recorded from L2/3 neurons in V1 slices (Fig. 6*C*), showing that this depolarized potential is caused by altered chloride equilibrium in gKO neurons.

The development of hyperpolarizing inhibition is accompanied by increased expression of KCC2, along with an increase in the ratio of KCC2/NKCC1 (21). To examine the expression of NKCC1 and KCC2, V1 tissue extracts were prepared from MeCP2 gKO and WT littermate control mice at P20–P25 and Western blot measurements were performed (Fig. 6*D*). KCC2 expression was

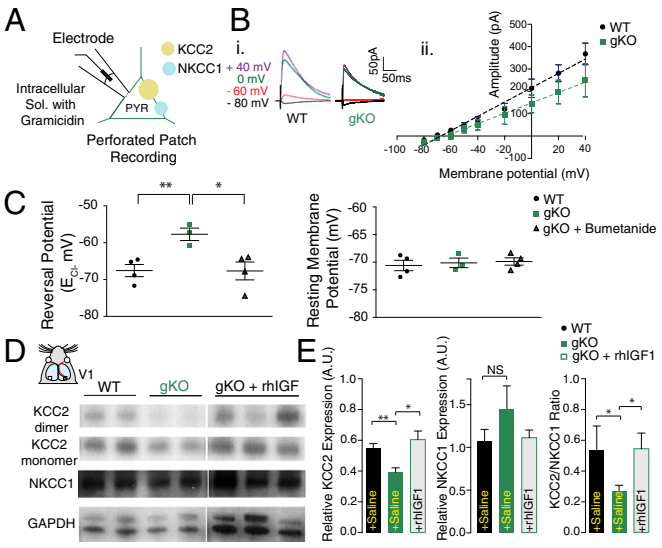

Fig. 6. Defective chloride signaling impacts inhibition in MeCP2-mutant mice. (*A–C*) Chloride reversal potential (E_{Cl}^-) remains depolarized in MeCP2 gKO mice during visual cortical development. (*A*) Cartoon showing perforated patch-clamp recording configuration in vitro from an L2/3 pyramidal neuron. The patch pipette is loaded with intracellular solution (Sol.) containing a pore-forming antibiotic, Gramicidin. (*B*, *i*) Recordings from representative V1 neurons in WT and gKO mice at several holding potentials. GABA responses shown at −80, −60, 0, and +40 mV were evoked by extracellular stimulation in the presence of glutamate receptor blockers D(−)-2-amino-5-phosphonovaleric acid (50 μM) and 2,3-dihydroxy-6-nitro-7-sulfamoyl-benzo[f]quinoxaline-2,3-dione (10 μM). (Scale bar: 50 ms, 50 pA.) (*B*, *ii*) E_{Cl}^- was calculated from the linear fit of the current–voltage relationship. (*C*) Individual recorded neurons show significantly depolarized chloride reversal potential in gKO mice, with no change in resting membrane potential. Selective NKCC1 inhibition upon systemic application of bumetanide restores E_{Cl}^- in gKO mice [P13–20: WT, $n = 4$ neurons from three mice; MeCP2 gKO, $n = 3$ neurons from three mice; MeCP2 gKO + Bumetanide (systemically treated animals with 100 μM bumetanide in bath), $n = 4$ neurons from two mice; $^{**}P < 0.01$, $^{*}P < 0.05$, by unpaired *t* test]. (*D* and *E*) Altered KCC2 expression in MeCP2 gKO mice and its rescue upon rhIGF1 administration. (*D*) Western blot measurements using V1 homogenates showing the expression profile of NKCC1 and KCC2 in WT mice, saline-treated MeCP2 gKO mice, and gKO mice treated with rhIGF1. (*E*) Relative KCC2 expression (normalized to GAPDH loading control) and KCC2/NKCC1 ratio are reduced in V1 of MeCP2 gKO mice. These reductions are rescued by the i.p. administration of rhIGF1. (P20–25: WT, $n = 4$ mice; MeCP2 gKO, $n = 4$ mice; MeCP2 gKO + rhIGF1, $n = 3$ mice). $^{*}P < 0.05$, $^{**}P < 0.01$; Student's *t* test). No difference in relative NKCC1 expression was observed between the two genotypes. $P > 0.05$, not significant (NS). All values are mean ± SEM. A.U., arbitrary units.

significantly lower in gKO mice compared with WT mice, with no difference in NKCC1 expression, so that the KCC2/NKCC1 ratio was lower in gKO mice (Fig. 6*E*). The KCC2 level and KCC2/NKCC1 ratio were also lower in the cortex of male MeCP2 gKO mice at an earlier age (P8) (Fig. S5). IGF1 has previously been shown to activate outward chloride transport during maturation of hippocampal neurons (30). Treatment of MeCP2 gKO mice with rhIGF1 for 7–10 d rescued the expression of KCC2 and restored the KCC2/NKCC1 ratio in rhIGF1-treated mice compared with age-matched, saline-treated gKO control mice (Fig. 6 *D* and *E*).

These results demonstrate a significant dysregulation of GABA as an inhibitory neurotransmitter in pyramidal neurons of MeCP2 gKO mice (Fig. S6) with reduced expression of KCC2, which is corrected by rhIGF1 treatment. Together with the effects of MeCP2 deletion on PV^+ neuron responses, these findings help explain the reduction of inhibition in gKO mice and rescue of its effects by rhIGF1.

Discussion

In this study, we describe five major results:

i) Global deletion of MeCP2 from all cells results in a reduction of visually driven excitatory and inhibitory conductances in V1 pyramidal neurons and alterations in their relative timing.

ii) PV^+ interneurons in mutant mice have reduced responses. When probed with natural scenes that activate V1 excitatory/inhibitory networks, pyramidal neurons in mutant mice also have reduced responses, together with reduced signal-to-noise ratio, reliability, and selectivity, as well as reduced interneuronal correlations.

iii) Deletion of MeCP2 from PV^+ neurons alone recapitulates effects of global MeCP2 deletion on pyramidal neurons.

iv) Loss of MeCP2 leads to reduced expression of the Cl^- exporter KCC2 and reduction of the KCC2/NKCC1 ratio, with altered GABA reversal potential in pyramidal neurons. Treatment with the NKCC1 inhibitor bumetanide restores the reversal potential.

v) Treatment of mutant mice with rhIGF1 restores PV^+ and pyramidal neuron responses, as well as KCC2 expression. These results demonstrate that reduction of both inhibition and excitation, importantly via MeCP2 effects on PV^+ neurons and KCC2, contributes to the cortical circuit deficits of RTT, and their joint restoration may be crucial for functionally correcting these deficits.

RTT is a neurodevelopmental disorder that primarily afflicts females (4). Affected females are initially asymptomatic, but later display a wide range of autonomic, cognitive, and motor symptoms with variable severity. Female *Mecp2* heterozygous mice display a robust but delayed and more variable phenotype than male hemizygous mice, and are crucially important for preclinical evaluation of effective therapeutic interventions (28, 74). Hemizygous male MeCP2 gKO mice display profound severity in various autonomic, sensory/motor, and cognitive phenotypes starting early in postnatal life; they effectively model the human disorder congenital encephalopathy. Because *Mecp2* is an X-linked gene and we focused our study on revealing cell-specific mechanisms that contribute to deficits in sensory processing and plasticity, we used male gKO mice to restrict mutations to defined cell populations and dissect the contributions of individual cell types to specific phenotypes. Further studies are necessary to confirm similar deficits in *Mecp2* heterozygous female mice and their amelioration with comparable treatments.

Role of Inhibition in RTT. Loss of MeCP2 from a subset of forebrain GABAergic neurons recapitulates diverse and prominent features of RTT (18), and the behavioral symptoms of MeCP2 loss can be explained by PV- or SOM-specific MeCP2 deletion (55). Furthermore, interneuron-specific reexpression of MeCP2 can ameliorate some of the deficits seen in RTT (19, 75). Our findings show that excitatory conductances are reduced concurrently with inhibitory conductances upon MeCP2 deletion. Reduced excitation accompanying inhibition within adult cortical circuits in vivo is consistent with previous findings in slices demonstrating reduced excitatory glutamatergic synapse number and weaker synaptic connections or drive in pyramidal neurons (76–79). Anatomical measurements have suggested increased PV^+ puncta, accelerated maturation of NMDA receptor subunit GluN2A, and enhanced perisomatic innervation in MeCP2 mutant mice (70, 71, 80), although another report found no change in PV^+ puncta in adult PV-MeCP2 mutant mice (81). At the same time, GABA and GAD65 levels are reduced in visual cortex (71). Our in vivo functional measurements of inhibitory conductances in adult MeCP2 gKO mice, along with targeted cell-specific recordings of PV^+ neurons, consistently reveal reduced inhibition or reduced inhibitory neuronal responses in

adult cortical circuits. Furthermore, our measurements of reduced visually driven excitatory conductances demonstrate that reduced visual responses of V1 pyramidal neurons or reduced propagated activity in slices in MeCP2 mutant mice (70, 71) are likely due not to increased inhibition but to reduced feedforward and recurrent excitatory drive, both of which are crucial elements of cortical circuits (82, 83).

PV^+ neuron-specific MeCP2 deletion leads to cell-autonomous effects, including immature membrane and synaptic properties in PV^+ cells (81). However, we also find profound non–cell-autonomous deficits in pyramidal neuron responses in PV-cKO mice; indeed, PV^+ cells are crucial for propagating the effects of MeCP2 reduction as a consequence of their role in visually driven regulation of E/I balance through PV/pyramidal networks (48, cf. 20). SOM^+ cells, on the other hand, may function as integrators of top-down inputs that modulate visual processing (11). Our finding that OD plasticity extends into adulthood is consistent with a reduction in inhibition received by pyramidal neurons, and with a recent report that OD plasticity after PV-specific MeCP2 deletion can be initiated by enhancing inhibition via intracerebral infusion of the $GABA_A$ receptor agonist diazepam (81).

Alterations in the Nature of Inhibition in RTT. Neuronal cation-chloride cotransporters play a key role in GABAergic circuit maturation (21, 22). Here, we present evidence that the loss of MeCP2 alters KCC2/NKCC1 ratio by a down-regulation of KCC2 expression (Fig. S6) that renders GABAergic synapses depolarizing with less effective inhibition in the cortex. Crucially, restoring the KCC2/NKCC1 ratio by bumetanide treatment restores the GABA polarity and reversal potential. It is possible that the hyperconnectivity of PV^+ neurons that is seen in MeCP2 gKO mice is a homeostatic response to this reduced inhibitory tone (71). A similar KCC2 deficiency in cornu ammonis 1 (CA1) pyramidal neurons leads to formation of hypertrophic PV^+ baskets adjacent to the sclerotic areas of patients with an epileptic hippocampus (84). Alterations of chloride cotransporters and aberrant GABAergic hyperinnervation can lead to an increased propensity for seizures, a prominent signature in ASDs, including RTT (85–87), which is also seen in mouse models of RTT (18–20).

Critical period plasticity in the visual cortex is influenced importantly by inhibitory GABAergic transmission and BDNF signaling (45, 88). Alterations in the polarity of GABAergic inhibition during early postnatal development through the NKCC1 antagonist bumetanide have been shown to prolong the duration of critical period plasticity in rat V1 (26). This effect can be rescued by concurrently increasing BDNF signaling by pharmacological means. Although the actual mechanisms that control the developmental expression of chloride cotransporters are not clear, MeCP2 is known to regulate neuronal activity-dependent expression of BDNF (27), which promotes the developmental up-regulation of KCC2 (89) and the maturation of cortical inhibition (88). Overexpression of KCC2 in MeCP2-deficient human neurons differentiated from induced pluripotent stem cells from patients with RTT has recently been shown to rescue GABA functional deficits (90). Neuronal Cl^- regulation through KCC2 thus offers an attractive target for postsynaptic modulation of inhibition in RTT.

Consistent with our findings in MeCP2 mutant mice, recent observations indicate that neuronal Cl^- regulation via the US Food and Drug Administration-approved diuretic bumetanide may provide a novel target-selective therapy for GABAergic dysfunction in neurodevelopmental disorders (23, 24, 73, 91; but see refs. 92 and 93). Independent of its Cl^- transport function, KCC2 also plays a key role in the development of excitatory synapses by mediating structural interactions with the actin cytoskeleton, contributing to the morphogenesis and maturation of dendritic spines (94). KCC2 may thus act as a synchronizing "hub" in the functional development of GABAergic as well as glutamatergic synapses, and act together with the non–cell-autonomous effects of PV^+ neurons to mediate the dual effects on inhibition and excitation caused by loss of MeCP2.

Unreliable Processing of Visual Information in RTT. A neuron's responses to visual stimuli directly reflect the circuits within which the neuron is embedded, and responses of V1 neurons in mutant mice thus provide sensitive assays of circuit dysfunction. Deleting MeCP2 globally or from PV^+ neurons causes a significant increase in response variability (reduced signal-to-noise ratio) to oriented gratings or natural movies and a reduction in response reliability to natural movies. The effects of deleting MeCP2 from SOM^+ neurons are less severe. It is likely that altered inhibition and excitation following MeCP2 deletion contribute fundamentally to these circuit-wide phenomena. The precise timing between excitatory and inhibitory synaptic currents is responsible for reliable spiking (12, 43). Loss of MeCP2 significantly alters the timing of E and I conductances, thereby directly contributing to altered spike reliability. Furthermore, changes in the magnitude of the summed E/I ratio impacts responsiveness and sparseness over the stimulus duration.

The accuracy of information encoding in the cortex depends not only on the response properties of individual neurons but also on the structure and magnitude of correlations between neurons (95). We demonstrate that deleting MeCP2 from PV^+ neurons, or globally from all cells, significantly decorrelates the network. These results are consistent with recent studies that have demonstrated reduced visual processing reliability in human subjects with autism (96). Thus, a decrease in visual processing efficiency may represent a fundamental physiological signature of neural processing in ASDs.

rhIGF1 Improves Cell-Specific and Circuit-Dependent Responses. IGF is known to activate key signaling pathways and prime the development and maturation of V1 neurons in mouse (97) and rat (98) visual cortex. IGF1 mRNA is reduced in the brain of MeCP2 gKO mice (99), and IGF1 levels are reduced in serum of MeCP2 gKO mice (28) and in cerebrospinal fluid of patients with RTT (100). rhIGF1 application enhances multiple components of the PI3K/AKT and ERK signaling pathways; increases PSD-95 at excitatory synapses; and enhances excitatory synaptic transmission in $Mecp2^{-/y}$ mice, curtails abnormally prolonged OD plasticity in adult $Mecp2^{-/+}$ mice, and ameliorates behavioral and organismal deficits in adult $Mecp2^{-/y}$ and $Mecp2^{-/+}$ mice (28). The signaling and synaptic effects of rhIGF1 may be useful for treating other ASDs, as demonstrated in both human IPSC-derived neurons (101) as well as mouse models (102).

The IGF1 receptor is widely distributed in the cortex (103) and, as we show here, is present on both excitatory and inhibitory neurons in V1. $Igf1^{-/-}$ mice have reduced numbers of PV^+ immunopositive neurons in the cortex and CA regions of the hippocampus, indicating that IGF1 has an important role in the development and maturation of PV^+ circuits in the brain (104). A recent study has revealed *Igf1* as a key activity-regulated gene in vasoactive intestinal peptide $(VIP)^+$ inhibitory interneurons, which, in turn, influence net inhibition onto cortical pyramidal neurons (105). Furthermore, IGF1 promotes maturation of Cl^- export and GABA hyperpolarization in CA1 neurons (30) and accelerates the developmental switch between NKCC1 and KCC2 chloride transporters in rat visual cortex (98). Our results demonstrate that rhIGF1 treatment in MeCP2 mutant mice improves not only PV^+ responses but also cell-specific and circuit-dependent responses of pyramidal neurons, likely via multiple mechanisms that jointly target inhibition and excitation. More broadly, such approaches may be crucial for addressing neurodevelopmental disorders where homeostatic and compensatory regulation accompanies constitutive loss or mutant protein expression (106).

Materials and Methods

Detailed information on all items below is provided in *SI Materials and Methods*.

Mice. All experiments were carried out under protocols approved by the Massachusetts Institute of Technology's Committee on Animal Care and conformed to NIH guidelines. *Mecp2*$^{-/y}$ hemizygous KO mice and WT littermates were obtained by breeding *Mecp2*$^{+/-}$ heterozygous females (107) with WT male mice. Neuronal subtype-specific deletion of MeCP2 was achieved by crossing cell type-specific Cre-driver lines (PV-Cre, SOM-IRES-Cre, and Camk2a-Cre) with homozygous Flox-MeCP2 female mice. WT C57 and floxed-MeCP2 male mice served as additional controls. All mice belonged to the C57BL6/J strain.

In Vivo Whole-Cell Electrophysiology. A small craniotomy (>0.5-mm diameter) was performed over V1, and the dura was removed. The brain was covered with artificial cerebrospinal fluid, and blind patch recording was performed to target L2/3 neurons of V1. For some of the recordings, 0.5% biocytin (wt/wt) was added to the intracellular solution to reconstruct the neuronal morphology.

In Vivo Two-Photon–Guided Cell-Attached Recordings. A borosilicate pipette (resistance of 3–7 MΩ, filled with Alexa Fluor 488) was inserted into the brain, and cells were targeted by moving the pipette diagonally through the cortex. Cell proximity was detected through deflections in resistance observed in voltage-clamp during a rapidly time-varying 5-mV command voltage pulse. Recordings were made using custom software (Network Prism; M.S. laboratory) written in MATLAB (MathWorks) controlling a MultiClamp 700B amplifier (Axon). All recorded cells were located in cortical L2/3 of V1.

In Vitro Perforated Patch Recording. Perforated patch recordings were made in vitro from L2/3 pyramidal neurons in V1 slices. Glass pipettes (resistance of 3–4 MΩ) were filled with a cesium-based intracellular solution. Recordings were made with freshly prepared gramicidin (stock solution prepared in DMSO: 50 mg/mL, final concentration of 50 μg/mL). Once giga-ohm seal configuration was achieved, gramicidin was allowed to diffuse for perforation for 15–20 min. Responses were elicited by intracortical electrical stimulation in L4, and GABA-mediated responses were recorded while the membrane voltage was clamped at various holding potentials.

Intrinsic Signal Optical Imaging. Mice (P28–30 and P56–60) were anesthetized with urethane (1.5 mg/g, i.p.) and chlorprothixene (10 mg/kg, i.p.). A custom-made head plate was glued to the skull to stabilize the head, and the cortex was covered with agarose solution [1.5% (wt/vol)] with a glass coverslip on top. Red light (630 nm) was used to illuminate the cortical surface, and the change of luminance was captured by a custom-built system during the presentation of visual stimuli (STIM; PsychToolbox).

In Vivo Two-Photon Ca^{2+} Imaging. Following a craniotomy, the synthetic calcium indicator OGB-1 AM (Invitrogen), dissolved in 20% (vol/vol) Pluronic F-127/DMSO (Invitrogen), was pressure-injected 180–200 μm below the pial surface using a picospritzer. A small glass coverslip (Warner Instruments) was implanted directly over the exposed cortex. The excitation laser was tuned to 960 nm, and imaging was performed through an Olympus XL Plan N Objective (magnification of 25×, N.A. = 1.05). All data were analyzed offline using custom-written scripts in MATLAB.

Systemic Administration of rhIGF1 and Bumetanide. Animals were injected i.p. once daily for 10–14 d with either vehicle (saline) or rhIGF1 (2.5 mg/kg; Peprotech) dissolved in saline with 0.01% BSA (wt/vol). Bumetanide (Sigma) was injected i.p. (0.2 mg/kg) daily for 3–4 d starting at P10. The injection solution was made in 2% DMSO dissolved in saline.

Western Blot. Protein samples were collected from dissected mouse cortex or V1 tissue with lysis buffer, sonicated, centrifuged, and separated on NuPAGE 4–12% Bis-Tris gel and transferred to PVDF membrane. The PVDF membrane was blocked and incubated overnight at 4 °C with primary antibodies followed by secondary HRP antibodies. Relative KCC2 and NKCC1 expression was calculated by normalizing protein signal to GAPDH or tubulin loading control.

Statistical Analysis. Nonparametric one-way ANOVA (Kruskal–Wallis test) was performed to determine statistical significance between experimental conditions. Further comparisons were made relative to WT data using Bonferroni-corrected rank-sum tests.

ACKNOWLEDGMENTS. We thank Jonathan Woodson, Chuong Le, Esmeralda Romero, Jorge Castro, Eric Wengert, Jitendra Sharma, and Nathan Wilson for varied assistance and discussion and Travis Emery for technical support. This work is supported by a postdoctoral fellowship from the Simons Center for the Social Brain (to A.B.), a predoctoral fellowship from Howard Hughes Medical Institute (to R.V.R.), and grants from the NIH (Grants R01EY007023 and R01MH085802) and the Simons Foundation (to M.S.). The R.J. laboratory was supported by a grant from the Simons Foundation and by grants from the NIH (Grants HD 045022 and R37-CA084198).

1. Sahin M, Sur M (2015) Genes, circuits, and precision therapies for autism and related neurodevelopmental disorders. *Science* 350(6263):aab3897.
2. Rubenstein JL, Merzenich MM (2003) Model of autism: Increased ratio of excitation/inhibition in key neural systems. *Genes Brain Behav* 2(5):255–267.
3. Zoghbi HY (2003) Postnatal neurodevelopmental disorders: Meeting at the synapse? *Science* 302(5646):826–830.
4. Chahrour M, Zoghbi HY (2007) The story of Rett syndrome: From clinic to neurobiology. *Neuron* 56(3):422–437.
5. Guy J, Cheval H, Selfridge J, Bird A (2011) The role of MeCP2 in the brain. *Annu Rev Cell Dev Biol* 27:631–652.
6. Lyst MJ, Bird A (2015) Rett syndrome: A complex disorder with simple roots. *Nat Rev Genet* 16(5):261–275.
7. Francke U (2006) Mechanisms of disease: Neurogenetics of MeCP2 deficiency. *Nat Clin Pract Neurol* 2(4):212–221.
8. McGraw CM, Samaco RC, Zoghbi HY (2011) Adult neural function requires MeCP2. *Science* 333(6039):186.
9. Banerjee A, Castro J, Sur M (2012) Rett syndrome: Genes, synapses, circuits, and therapeutics. *Front Psychiatry* 3:34.
10. Lioy DT, et al. (2011) A role for glia in the progression of Rett's syndrome. *Nature* 475(7357):497–500.
11. Hangya B, Pi HJ, Kvitsiani D, Ranade SP, Kepecs A (2014) From circuit motifs to computations: Mapping the behavioral repertoire of cortical interneurons. *Curr Opin Neurobiol* 26:117–124.
12. Isaacson JS, Scanziani M (2011) How inhibition shapes cortical activity. *Neuron* 72(2):231–243.
13. Kepecs A, Fishell G (2014) Interneuron cell types are fit to function. *Nature* 505(7483):318–326.
14. Wilson NR, Runyan CA, Wang FL, Sur M (2012) Division and subtraction by distinct cortical inhibitory networks in vivo. *Nature* 488(7411):343–348.
15. Atallah BV, Bruns W, Carandini M, Scanziani M (2012) Parvalbumin-expressing interneurons linearly transform cortical responses to visual stimuli. *Neuron* 73(1):159–170.
16. Adesnik H, Bruns W, Taniguchi H, Huang ZJ, Scanziani M (2012) A neural circuit for spatial summation in visual cortex. *Nature* 490(7419):226–231.
17. Lee SH, et al. (2012) Activation of specific interneurons improves V1 feature selectivity and visual perception. *Nature* 488(7411):379–383.
18. Chao HT, et al. (2010) Dysfunction in GABA signalling mediates autism-like stereotypies and Rett syndrome phenotypes. *Nature* 468(7321):263–269.
19. Goffin D, Brodkin ES, Blendy JA, Siegel SJ, Zhou Z (2014) Cellular origins of auditory event-related potential deficits in Rett syndrome. *Nat Neurosci* 17(6):804–806.
20. Zhang W, Peterson M, Beyer B, Frankel WN, Zhang ZW (2014) Loss of MeCP2 from forebrain excitatory neurons leads to cortical hyperexcitation and seizures. *J Neurosci* 34(7):2754–2763.
21. Blaesse P, Airaksinen MS, Rivera C, Kaila K (2009) Cation-chloride cotransporters and neuronal function. *Neuron* 61(6):820–838.
22. Kaila K, Price TJ, Payne JA, Puskarjov M, Voipio J (2014) Cation-chloride cotransporters in neuronal development, plasticity and disease. *Nat Rev Neurosci* 15(10):637–654.
23. Ben-Ari Y (2015) Is birth a critical period in the pathogenesis of autism spectrum disorders? *Nat Rev Neurosci* 16(8):498–505.
24. He Q, Nomura T, Xu J, Contractor A (2014) The developmental switch in GABA polarity is delayed in fragile X mice. *J Neurosci* 34(2):446–450.
25. Duarte ST, et al. (2013) Abnormal expression of cerebrospinal fluid cation chloride cotransporters in patients with Rett syndrome. *PLoS One* 8(7):e68851.
26. Deidda G, et al. (2015) Early depolarizing GABA controls critical-period plasticity in the rat visual cortex. *Nat Neurosci* 18(1):87–96.
27. Chen WG, et al. (2003) Derepression of BDNF transcription involves calcium-dependent phosphorylation of MeCP2. *Science* 302(5646):885–889.
28. Castro J, et al. (2014) Functional recovery with recombinant human IGF1 treatment in a mouse model of Rett Syndrome. *Proc Natl Acad Sci USA* 111(27):9941–9946.
29. Tropea D, et al. (2009) Partial reversal of Rett Syndrome-like symptoms in MeCP2 mutant mice. *Proc Natl Acad Sci USA* 106(6):2029–2034.
30. Kelsch W, et al. (2001) Insulin-like growth factor 1 and a cytosolic tyrosine kinase activate chloride outward transport during maturation of hippocampal neurons. *J Neurosci* 21(21):8339–8347.
31. Rett A (1992) The mystery of the Rett syndrome. *Brain Dev* 14(Suppl):S141–S142.
32. Hagberg B (1992) The Rett syndrome: An introductory overview 1990. *Brain Dev* 14 (Suppl):S5–S8.
33. von Tetzchner S, et al. (1996) Vision, cognition and developmental characteristics of girls and women with Rett syndrome. *Dev Med Child Neurol* 38(3):212–225.
34. Stauder JE, Smeets EE, van Mil SG, Curfs LG (2006) The development of visual- and auditory processing in Rett syndrome: An ERP study. *Brain Dev* 28(8):487–494.
35. LeBlanc JJ, et al. (2015) Visual evoked potentials detect cortical processing deficits in Rett syndrome. *Ann Neurol* 78(5):775–786.
36. Rose SA, et al. (2013) Rett syndrome: An eye-tracking study of attention and recognition memory. *Dev Med Child Neurol* 55(4):364–371.

37. Hubel DH, Wiesel TN (1959) Receptive fields of single neurones in the cat's striate cortex. *J Physiol* 148:574–591.
38. Carandini M, Heeger DJ (2011) Normalization as a canonical neural computation. *Nat Rev Neurosci* 13(1):51–62.
39. Vinje WE, Gallant JL (2000) Sparse coding and decorrelation in primary visual cortex during natural vision. *Science* 287(5456):1273–1276.
40. Haider B, et al. (2010) Synaptic and network mechanisms of sparse and reliable visual cortical activity during nonclassical receptive field stimulation. *Neuron* 65(1):107–121.
41. Rikhye RV, Sur M (2015) Spatial correlations in natural scenes modulate response reliability in mouse visual cortex. *J Neurosci* 35(43):14661–14680.
42. Haider B, Häusser M, Carandini M (2013) Inhibition dominates sensory responses in the awake cortex. *Nature* 493(7430):97–100.
43. Wehr M, Zador AM (2003) Balanced inhibition underlies tuning and sharpens spike timing in auditory cortex. *Nature* 426(6965):442–446.
44. Espinosa JS, Stryker MP (2012) Development and plasticity of the primary visual cortex. *Neuron* 75(2):230–249.
45. Hensch TK (2005) Critical period plasticity in local cortical circuits. *Nat Rev Neurosci* 6(11):877–888.
46. Hübener M, Bonhoeffer T (2014) Neuronal plasticity: Beyond the critical period. *Cell* 159(4):727–737.
47. Sengpiel F, Kind PC (2002) The role of activity in development of the visual system. *Curr Biol* 12(23):R818–R826.
48. Xue M, Atallah BV, Scanziani M (2014) Equalizing excitation-inhibition ratios across visual cortical neurons. *Nature* 511(7511):596–600.
49. Marchetto MC, et al. (2010) A model for neural development and treatment of Rett syndrome using human induced pluripotent stem cells. *Cell* 143(4):527–539.
50. Li Y, et al. (2013) Global transcriptional and translational repression in human-embryonic-stem-cell-derived Rett syndrome neurons. *Cell Stem Cell* 13(4):446–458.
51. Niell CM, Stryker MP (2008) Highly selective receptive fields in mouse visual cortex. *J Neurosci* 28(30):7520–7536.
52. Runyan CA, Sur M (2013) Response selectivity is correlated to dendritic structure in parvalbumin-expressing inhibitory neurons in visual cortex. *J Neurosci* 33(28): 11724–11733.
53. del Río JA, de Lecea L, Ferrer I, Soriano E (1994) The development of parvalbumin-immunoreactivity in the neocortex of the mouse. *Brain Res Dev Brain Res* 81(2):247–259.
54. Gonchar Y, Wang Q, Burkhalter A (2008) Multiple distinct subtypes of GABAergic neurons in mouse visual cortex identified by triple immunostaining. *Front Neuroanat* 1:3.
55. Ito-Ishida A, Ure K, Chen H, Swann JW, Zoghbi HY (2015) Loss of MeCP2 in parvalbumin-and somatostatin-expressing neurons in mice leads to distinct Rett syndrome-like phenotypes. *Neuron* 88(4):651–658.
56. Runyan CA, et al. (2010) Response features of parvalbumin-expressing interneurons suggest precise roles for subtypes of inhibition in visual cortex. *Neuron* 67(5):847–857.
57. Zariwala HA, et al. (2011) Visual tuning properties of genetically identified layer 2/3 neuronal types in the primary visual cortex of cre-transgenic mice. *Front Syst Neurosci* 4:162.
58. Kerlin AM, Andermann ML, Berezovskii VK, Reid RC (2010) Broadly tuned response properties of diverse inhibitory neuron subtypes in mouse visual cortex. *Neuron* 67(5):858–871.
59. Cottam JC, Smith SL, Häusser M (2013) Target-specific effects of somatostatin-expressing interneurons on neocortical visual processing. *J Neurosci* 33(50):19567–19578.
60. Ma WP, et al. (2010) Visual representations by cortical somatostatin inhibitory neurons–selective but with weak and delayed responses. *J Neurosci* 30(43):14371–14379.
61. Vogelstein JT, et al. (2010) Fast nonnegative deconvolution for spike train inference from population calcium imaging. *J Neurophysiol* 104(6):3691–3704.
62. Baudot P, et al. (2013) Animation of natural scene by virtual eye-movements evokes high precision and low noise in V1 neurons. *Front Neural Circuits* 7:206.
63. Pecka M, Han Y, Sader E, Mrsic-Flogel TD (2014) Experience-dependent specialization of receptive field surround for selective coding of natural scenes. *Neuron* 84(2): 457–469.
64. Ko H, et al. (2011) Functional specificity of local synaptic connections in neocortical networks. *Nature* 473(7345):87–91.
65. Cohen MR, Kohn A (2011) Measuring and interpreting neuronal correlations. *Nat Neurosci* 14(7):811–819.
66. Gordon JA, Stryker MP (1996) Experience-dependent plasticity of binocular responses in the primary visual cortex of the mouse. *J Neurosci* 16(10):3274–3286.
67. Kuhlman SJ, et al. (2013) A disinhibitory microcircuit initiates critical-period plasticity in the visual cortex. *Nature* 501(7468):543–546.
68. Pizzorusso T, et al. (2002) Reactivation of ocular dominance plasticity in the adult visual cortex. *Science* 298(5596):1248–1251.
69. Harauzov A, et al. (2010) Reducing intracortical inhibition in the adult visual cortex promotes ocular dominance plasticity. *J Neurosci* 30(1):361–371.
70. Krishnan K, et al. (2015) MeCP2 regulates the timing of critical period plasticity that shapes functional connectivity in primary visual cortex. *Proc Natl Acad Sci USA* 112(34):E4782–E4791.
71. Durand S, et al. (2012) NMDA receptor regulation prevents regression of visual cortical function in the absence of Mecp2. *Neuron* 76(6):1078–1090.
72. Sugiyama S, et al. (2008) Experience-dependent transfer of Otx2 homeoprotein into the visual cortex activates postnatal plasticity. *Cell* 134(3):508–520.
73. Deidda G, et al. (2015) Reversing excitatory GABAAR signaling restores synaptic plasticity and memory in a mouse model of Down syndrome. *Nat Med* 21(4):318–326.
74. Samaco RC, et al. (2013) Female Mecp2(+/-) mice display robust behavioral deficits on two different genetic backgrounds providing a framework for pre-clinical studies. *Hum Mol Genet* 22(1):96–109.
75. Ure K, et al. (2016) Restoration of Mecp2 expression in GABAergic neurons is sufficient to rescue multiple disease features in a mouse model of Rett syndrome. *eLife* 5:e14198.
76. Chao HT, Zoghbi HY, Rosenmund C (2007) MeCP2 controls excitatory synaptic strength by regulating glutamatergic synapse number. *Neuron* 56(1):58–65.
77. Dani VS, et al. (2005) Reduced cortical activity due to a shift in the balance between excitation and inhibition in a mouse model of Rett syndrome. *Proc Natl Acad Sci USA* 102(35):12560–12565.
78. Wood L, Gray NW, Zhou Z, Greenberg ME, Shepherd GM (2009) Synaptic circuit abnormalities of motor-frontal layer 2/3 pyramidal neurons in an RNA interference model of methyl-CpG-binding protein 2 deficiency. *J Neurosci* 29(40):12440–12448.
79. Dani VS, Nelson SB (2009) Intact long-term potentiation but reduced connectivity between neocortical layer 5 pyramidal neurons in a mouse model of Rett syndrome. *J Neurosci* 29(36):11263–11270.
80. Mierau SB, Patrizi A, Hensch TK, Fagiolini M (2016) Cell-specific regulation of N-methyl-D-aspartate receptor maturation by Mecp2 in cortical circuits. *Biol Psychiatry* 79(9):746–754.
81. He LJ, et al. (2014) Conditional deletion of Mecp2 in parvalbumin-expressing GABAergic cells results in the absence of critical period plasticity. *Nat Commun* 5:5036.
82. Harris KD, Mrsic-Flogel TD (2013) Cortical connectivity and sensory coding. *Nature* 503(7474):51–58.
83. Harris KD, Shepherd GM (2015) The neocortical circuit: Themes and variations. *Nat Neurosci* 18(2):170–181.
84. Muñoz A, Méndez P, DeFelipe J, Alvarez-Leefmans FJ (2007) Cation-chloride cotransporters and GABA-ergic innervation in the human epileptic hippocampus. *Epilepsia* 48(4):663–673.
85. Canitano R (2007) Epilepsy in autism spectrum disorders. *Eur Child Adolesc Psychiatry* 16(1):61–66.
86. Glaze DG, et al. (2010) Epilepsy and the natural history of Rett syndrome. *Neurology* 74(11):909–912.
87. Karlócai MR, et al. (2016) Enhanced expression of potassium-chloride cotransporter KCC2 in human temporal lobe epilepsy. *Brain Struct Funct* 221(7):3601–3615.
88. Huang ZJ, et al. (1999) BDNF regulates the maturation of inhibition and the critical period of plasticity in mouse visual cortex. *Cell* 98(6):739–755.
89. Ludwig A, et al. (2011) Early growth response 4 mediates BDNF induction of potassium chloride cotransporter 2 transcription. *J Neurosci* 31(2):644–649.
90. Tang X, et al. (2016) KCC2 rescues functional deficits in human neurons derived from patients with Rett syndrome. *Proc Natl Acad Sci USA* 113(3):751–756.
91. Maa EH, Kahle KT, Walcott BP, Spitz MC, Staley KJ (2011) Diuretics and epilepsy: will the past and present meet? *Epilepsia* 52(9):1559–1569.
92. O'Donnell ME (1993) Role of Na-K-Cl cotransport in vascular endothelial cell volume regulation. *Am J Physiol* 264(5 Pt 1):C1316–C1326.
93. Pressler RM, et al.; NEonatal seizure treatment with Medication Off-patent (NEMO) consortium (2015) Bumetanide for the treatment of seizures in newborn babies with hypoxic ischaemic encephalopathy (NEMO): An open-label, dose finding, and feasibility phase 1/2 trial. *Lancet Neurol* 14(5):469–477.
94. Li H, et al. (2007) KCC2 interacts with the dendritic cytoskeleton to promote spine development. *Neuron* 56(6):1019–1033.
95. Shadlen MN, Newsome WT (1994) Noise, neural codes and cortical organization. *Curr Opin Neurobiol* 4(4):569–579.
96. Dinstein I, et al. (2012) Unreliable evoked responses in autism. *Neuron* 75(6):981–991.
97. Tropea D, et al. (2006) Gene expression changes and molecular pathways mediating activity-dependent plasticity in visual cortex. *Nat Neurosci* 9(5):660–668.
98. Baroncelli L, et al. (2016) Early IGF-1 primes visual cortex maturation and accelerates developmental switch between NKCC1 and KCC2 chloride transporters in enriched animals. *Neuropharmacology* 113:167–177.
99. Mellios N, et al. (2014) β2-Adrenergic receptor agonist ameliorates phenotypes and corrects microRNA-mediated IGF1 deficits in a mouse model of Rett syndrome. *Proc Natl Acad Sci USA* 111(27):9947–9952.
100. Khwaja OS, et al. (2014) Safety, pharmacokinetics, and preliminary assessment of efficacy of mecasermin (recombinant human IGF-1) for the treatment of Rett syndrome. *Proc Natl Acad Sci USA* 111(12):4596–4601.
101. Shcheglovitov A, et al. (2013) SHANK3 and IGF1 restore synaptic deficits in neurons from 22q13 deletion syndrome patients. *Nature* 503(7475):267–271.
102. Bozdagi O, Tavassoli T, Buxbaum JD (2013) Insulin-like growth factor-1 rescues synaptic and motor deficits in a mouse model of autism and developmental delay. *Mol Autism* 4(1):9.
103. Fernandez AM, Torres-Alemán I (2012) The many faces of insulin-like peptide signalling in the brain. *Nat Rev Neurosci* 13(4):225–239.
104. Beck KD, Powell-Braxton L, Widmer HR, Valverde J, Hefti F (1995) Igf1 gene disruption results in reduced brain size, CNS hypomyelination, and loss of hippocampal granule and striatal parvalbumin-containing neurons. *Neuron* 14(4):717–730.
105. Mardinly AR, et al. (2016) Sensory experience regulates cortical inhibition by inducing IGF1 in VIP neurons. *Nature* 531(7594):371–375.
106. Nelson SB, Valakh V (2015) Excitatory/inhibitory balance and circuit homeostasis in autism spectrum disorders. *Neuron* 87(4):684–698.
107. Guy J, Hendrich B, Holmes M, Martin JE, Bird A (2001) A mouse Mecp2-null mutation causes neurological symptoms that mimic Rett syndrome. *Nat Genet* 27(3):322–326.

Supporting Information

Banerjee et al. 10.1073/pnas.1615330113

SI Materials and Methods

Mice. All experiments were carried out under protocols approved by MIT's Committee on Animal Care and conformed to NIH guidelines.

Mecp2$^{-/y}$ hemizygous KO mice and WT littermates were obtained by breeding *Mecp2*$^{-/+}$ heterozygous females (107) on a C57BL/6 background with WT male mice on the same background. Neuronal subtype-specific deletion of MeCP2 was achieved by crossing cell type-specific Cre-driver lines (PV-Cre, Jackson ID: 017320; and SOM-IRES-Cre) with homozygous female mice carrying two functional loxP sites flanking exons 3–4 of MeCP2 on the X-chromosome (B6.129P2-Mecp2^{tm1Bird}/J or Flox-MeCP2; Jackson ID: 007177) (107). Male mice were used in all experiments. To delete MeCP2 specifically in PV$^+$ inhibitory interneurons, *PV-Mecp2*$^{-/y}$ (or PV-cKO) mice were used, which were generated by breeding homozygous female Flox-MeCP2 mice with PV-Cre knock-in homozygous male mice (generated by Silvia Arber, Friedrich Miescher Institute, Basel, Switzerland). Similarly, *SOM-Mecp2*$^{-/y}$ (or SOM-cKO) mice were obtained by breeding homozygous Flox-MeCP2 female mice with SOM-IRES-Cre knock-in homozygous male mice (generated by J. Z. Huang, Cold Spring Harbor Laboratory, Cold Spring Harbor, NY; Jackson ID: 013044) to achieve specific deletion of MeCP2 in SOM$^+$ interneurons. Excitatory neuron-specific MeCP2 deletion was achieved by crossing homozygous Flox-MeCP2 females with homozygous Camk2a-Cre males (Jackson ID: 005359). Male Flox-MeCP2 animals were used as controls. We also crossed PV- and SOM-Cre male mice with *Mecp2*$^{+/-}$ heterozygous females, took F1 animals, and genotyped for -Cre$^+$ and MeCP2 allele. We used these mice to compare effects of MeCP2 deletion on PV$^+$ and SOM$^+$ response properties in a gKO background compared with cKO mice. MeCP2 gKO and their WT littermate control animals were compared in non-cell type targeted recordings (Fig. 1) and in patch-clamp recordings in slices and Western blots (Fig. 6). PV- and SOM-cKO animals were used for two-photon targeted patch recordings (Figs. 1, 2, and 5), and compared with mice in which Cre-recombinase was expressed under PV or SOM promoter (PV- or SOM-Cre), because Cre-recombinase is essential for Cre-dependent RFP expression. WT C57 and floxed-MeCP2 animals served as additional controls in Figs. 3–5 and Fig. S3.

Mice were grouped with their WT siblings and housed at 24 °C and variable humidity in a 12-h dark/light cycle (7:00 AM to 7:00 PM). All mice belonged to the C57BL6/J strain.

Virus Injection. Three- to four-week-old mice were briefly anesthetized with isoflurane (3%) in oxygen in an anesthesia chamber and taken to the injection platform. The cranium was secured with ear bars, and anesthesia was maintained during surgery with 1.5–2.0% isoflurane. An L-shaped incision was made in the skin, and surface of the cranium was cleaned using absorbent swabs (Sugi; Kettenbach, GmbH). Injection coordinates were 3 mm lateral from bregma and 1 mm anterior from the posterior suture. The skull was thinned along a 1-mm line at the rostral edge of V1 using a dremel drill with occasional cooling with saline, and the remaining dura was punctured using a glass micropipette filled with the virus suspended in mineral oil.

To study cellular response properties, RFP was expressed in PV$^+$ and SOM$^+$ neurons in V1 of PV/SOM-Cre mice by infection of a lox-STOP-lox RFP construct packaged into adenoassociated virus (serotype 2/9) as described previously (56).

Three to four injections were made at neighboring sites at a depth of 200–250 μm. A volume of 200 nL of virus was injected at the rate of 75 nL·min^{-1} at each site. After each injection, the pipette was held in place for 3–5 min before retraction to prevent leakage. Skin was sutured using a synthetic, monofilament, nonabsorbable suture (Prolene 7.0; Ethicon).

In Vivo Experiments: Surgery. Two to three weeks after virus injection, mice were used for electrophysiology experiments. Mice were anesthetized using urethane (1.5 mg/g, i.p.) and chlorprothixene (10 mg/kg, i.p.). The eyes were protected with ophthalmic ointment during the surgery and moistened afterward with saline. The skin was excised and cleaned with Sugi, a metal head plate was attached to the skull using superglue and dental acrylic, and a 2-mm × 2-mm craniotomy was performed over V1 (area 17). The exposed area was then covered with a thin layer of agarose solution [1.5% (wt/vol)] in artificial cerebrospinal fluid [aCSF; 140 mM NaCl, 5 mM KCl, 2 mM $CaCl_2$, 1 mM $MgCl_2$, 0.01 mM EDTA, 10 mM Hepes, 10 mM glucose (pH 7.4)]. Head plates were screwed onto a moveable platform, and mice were transferred to the microscope. During the recording, additional anesthetic was injected as needed. Body temperature was maintained throughout surgery and the experiment at 37.5 °C with a heating blanket (Harvard Apparatus) and supplementary heating pads. Saline (0.9% NaCl) was injected multiple times during the whole experiment to hydrate the mouse. The recording phase of electrophysiology experiments typically lasted for about 4–6 h.

In Vivo Whole-Cell Electrophysiology. A small craniotomy (>0.5-mm diameter) was performed over V1. The dura was removed using fine forceps, making sure that the brain remained accessible. The brain was covered with aCSF containing 140 mM NaCl, 5 mM KCl, 2 mM $CaCl_2$, 1 mM $MgCl_2$, 0.01 mM EDTA, 10 mM Hepes, and 10 mM glucose. Patch pipettes (4–6 MΩ) were filled with a cesium (Cs)-based intracellular solution containing 125 mM Cs-methanesulfonate, 2 mM KCl, 10 mM Hepes, 4 mM Mg-ATP, 0.3 mM Na_2-GTP, 10 mM EGTA, 5 mM tetraethylammonium chloride (TEA-Cl), 8 mM Na_2-phosphocreatine, and 2 mM QX-314 (pH 7.3) at 290–295 mOsm. Access resistance was monitored throughout the recording period by applying a small (−10 mV) square pulse at the beginning of each visual stimulus trial. Cells with an access resistance exceeding 50 MΩ, or with access resistance varying more than 10% during the entire recording period, were discarded. The average access resistance was 38 ± 5 MΩ and 37 ± 3 MΩ in WT and MeCP2 gKO conditions, respectively. Excitatory and inhibitory conductances were isolated using the formula:

$$\Delta I = G_e(V - E_e) + G_i(V - E_i),$$

where ΔI is the current recorded at any time point after subtracting the average baseline current ($I - I_0$), G_e and G_i are the excitatory and inhibitory synaptic conductances, V is the holding voltage, and E_e and E_i are the reversal potentials for excitatory and inhibitory currents (+20 mV and −70 mV, respectively). The clamping voltage was corrected for the effective series resistance for each cell using:

$$V = V_h - R_s I,$$

where V_h is the applied holding voltage and R_s is the effective series resistance.

Blind patch recording was performed to target L2/3 neurons of V1. The position of each cell was monitored using the reading on the micromanipulator (Sutter Instruments). On average, cells from WT and MeCP2 were recorded at a depth of 220 ± 26 μm and 189 ± 11 μm, respectively. For some of the recordings, 0.5% biocytin (wt/wt) was added to the intracellular solution to reconstruct

the neuronal morphology. Animals were deeply anesthetized at the end of the experiment and transcardially perfused with 0.9% NaCl followed by 4% paraformaldehyde (PFA). One hundred-micrometer coronal sections of V1 were cut using a vibratome (Leica VT1200s). Slices were treated with 1% (wt/wt) Triton in PBS for 4 h and stained overnight with PBS + 0.1% Triton + 3% BSA + 1/200 Alexa 488-conjugated streptavidin (Lifescience). Neurons were imaged using a confocal microscope (Zeiss) and traced using the neurite tracer in ImageJ (NIH).

In Vivo Two-Photon–Guided Cell-Attached Recordings. Borosilicate pipettes (outer diameter = 1.5 mm, inner diameter = 1.17 mm; WPI) were pulled using a Sutter P-2000 laser puller (Sutter Instruments). Tip diameter was around 1 μm, whereas the resistance was between 3 and 7 MΩ. Recordings were made using custom software (Network Prism; M.S. laboratory) written in MATLAB (MathWorks) controlling a MultiClamp 700B amplifier (Axon). A glass pipette electrode was inserted into the brain at an angle of 20–35°, and an Ag/AgCl ground electrode pellet (Warner Instruments) was positioned in the same solution as the brain and the objective. For visualization, pipettes were filled with Alexa Fluor 488 (100 μM; Molecular Probes). The pipette was first targeted to the injection site using a 10× lens, and then targeted to individual cells using a 25× lens via simultaneous two-photon imaging at 770 or 920 nm. Cells were targeted by moving the pipette into the 3D vicinity and then commencing a diagonal advance, or cells were patched blindly by advancing diagonally through the cortex. While approaching a cell, either zero pressure or light positive pressure was applied. Cell proximity was detected through deflections in resistance observed in voltage-clamp during a rapidly time-varying 5-mV command voltage pulse. Once resistance had increased by 5–10 MΩ, slight negative pressure was applied and the pipette was advanced more slowly until resistance increased to 20–80 MΩ. At that point, the amplifier was switched to current-clamp, and spikes were recorded with zero injected current under a Bessel filter of 4 KHz and an alternating current (AC) filter of 300 Hz. All recorded cells were located in the superficial cortical layer (between 150 and 330 μm below the pial surface).

In Vitro Perforated Patch Recording. Perforated patch recordings were made in vitro from L2/3 pyramidal neurons in V1 slices prepared from MeCP2 gKO mice and WT littermate controls. Glass pipettes (resistance of 3–4 MΩ) were filled with a Cs-based intracellular solution containing 103 mM CsCl, 12 mM CsOH, 12 mM methanesulfonic acid, 4 mM NaCl, 5 mM TEA-Cl, 10 mM Hepes, 0.5 mM EGTA, 10 mM phosphocreatine, 5 mM lidocaine *N*-ethyl chloride, 4 mM ATP-magnesium salt, and 0.3 GTP-sodium salt. The pH was adjusted to 7.2–7.4 with KOH, and osmolality was adjusted to 295–300 mOsm. Recordings were made with gramicidin (stock solution prepared in DMSO: 50 mg/mL stored at 4 °C for up to 1 wk, final concentration of 50 μg/mL) to avoid dialysis of intracellular [Cl^-] concentration. Gramicidin-containing internal solution was freshly prepared, and recordings were performed within 1.5 h. To fill the recording pipette, the tip of the recording pipette was dipped into gramicidin-free internal solution for 5 s to facilitate sealing onto the neuron, followed by backfilling with internal solution with gramicidin. Care was taken to avoid air bubbles when adding gramicidin-containing internal solution. Very mild positive pressure was applied to the pipette to avoid gramicidin leaking out from the tip of the recording pipette. Once giga-ohm seal configuration was achieved, gramicidin was allowed to diffuse for perforation for 15–20 min. GABA-mediated responses were elicited by intracortical electrical stimulation in L4 and isolated by the application of antagonists of glutamatergic transmission [50 μM D(−)-2-amino-5-phosphonopentanoic acid and 10 μM 2,3-dihydroxy-6-nitro-7-sulfamoyl-benzo[f]quinoxaline-2,3-dione]. GABA-mediated responses were recorded while the membrane voltage was clamped at various holding potentials between −80 mV and +40 mV. All recordings were done at 32 °C.

For perforated patch recordings in the presence of bumetanide, bumetanide was dissolved in DMSO to make a stock solution (50 mM) that was then diluted (1:500), included in both cutting solution and aCSF, and bath-applied during slice electrophysiology. The recording procedure was followed as described above.

Eyelid Suture for MD. Critical period (P25–26) or adult (P56–57) mice were anesthetized using isoflurane. For MD, eyelid margins of the contralateral eye were trimmed and both upper and lower lids were sutured closed using a nonabsorbable suture (Prolene 7.0). Special care was taken to ensure that the eyelids remained closed for the duration of the deprivation paradigm (3–4 d). For in vivo optical imaging experiments, stitches were removed and eyes were reopened under anesthesia right before the experiment.

Intrinsic Signal Optical Imaging. Mice (P28–30 and P56–60) were anesthetized with urethane (1.5 mg/g, i.p.) and sedative chlorprothixene (10 mg/kg, i.p.). The skin was excised, and the skull was exposed over V1. A custom-made head plate was glued to the skull to stabilize the head and minimize movement. The skull was thinned over V1 for the older animals. The cortex was covered with agarose solution [1.5% (wt/vol)], and a glass coverslip was placed on top. During the imaging session, the animal's body temperature was kept constant with heating pads and the electrocardiogram was monitored constantly. Eyes were periodically treated with silicone oil, and pure oxygen was delivered through a tube. Red light (630 nm) was used to illuminate the cortical surface, and the change of luminance was captured by a CCD camera (Cascade 512B; Roper Scientific) during the presentation of visual stimuli (STIM; PsychToolbox). Custom software was developed to control the image acquisition and synchronization between the camera and stimuli. An elongated horizontal white bar (9° × 72°) over a uniformly gray background was drifted continuously vertically upward in the direction of the visual field. After moving to the last position, the bar would jump back to the initial position and start another cycle of movement; thus, the chosen region of visual space (72° × 72°) was stimulated in a periodic fashion (9 seconds per cycle). Images of the visual cortex were continuously captured at the rate of 15 frames per second during each stimulus session of 25 min. A temporal high-pass filter (135 frames) was used to remove slow noise components, after which the temporal fast Fourier transform (FFT) component at the stimulus frequency (9 s^{-1}) was calculated pixel-by-pixel from the whole set of images. No spatial averaging was done. The amplitude of the FFT component was used to measure the strength of the visually driven response for each eye, and the ODI was derived from each eye's ipsilateral (ipsi) or contralateral (contra) response (R) at each pixel as ODI = (Rcontra − Ripsi)/(Rcontra + Ripsi). The binocular zone was defined as the cortical region that was driven by inputs from both eyes.

In Vivo Two-Photon Ca^{2+} Imaging. Craniotomies were performed over binocular V1 as described above. The synthetic calcium indicator OGB-1 AM (Invitrogen) was dissolved in 20% (vol/vol) Pluronic F-127/DMSO (Invitrogen) for 25 min to a concentration of 10 mM. This solution was then diluted in sterile calcium-free PBS (pH 7.4; Invitrogen) to achieve a final concentration of 1 mM. In addition 100 μM Alexa Fluor 488 (Invitrogen) was added to the solution to visualize the pipette during the injection. Before injection, this solution was filtered with a 0.45-μm centrifugal filter. Following the craniotomy, the dye solution was pressure-injected 180–200 μm below the pial surface using a picospritzer. Typically, we used 10 psi for 1 min and repeated the injection at three to five slightly overlapping regions. Following this procedure, a small 4-mm-diameter glass coverslip (Warner Instruments) was implanted directly over the exposed cortex and sealed with a silicone elastomer (Kwik-Sil; WPI). This glass coverslip prevented large brain movements and allowed stable recording.

Imaging was performed using a Prairie Ultima two-photon system (Prairie Technologies) with a Spectra Physics Mai-Tai eHP laser coupled with a DeepSee module. The excitation laser was tuned to 960 nm, and imaging was performed through an Olympus XL Plan N Objective (magnification of 25×, N.A. = 1.05). We used custom-written MATLAB scripts (MathWorks) to detect neurons automatically, to define an optimized scan path, and to collect raster scans at ∼50 frames per second (14). All data were analyzed offline using custom-written scripts in MATLAB (*SI Materials and Methods*, *Data Analysis*).

Visual Stimulation. To assess the orientation selectivity and tuning of neurons, we presented oriented gratings on a 23-inch 1080p LCD monitor (Dell) using custom software (Network Visstim; M.S. laboratory) written in PsychToolbox-3 (Psychtoolbox.com) on a Windows 7 computer (Dell Precision) with a GeForce 8800 GTS 640-MB graphics card (PNY). Gratings were optimized for cellular responsiveness using a contrast of 100%, spatial frequency of 0.002–0.256 cycles per degree, and temporal frequency of 1–3 Hz. Gratings were then presented by stepping the orientation from 0–360° in steps of 20°, with each grating presentation being preceded for 4 s "off" followed by 4 s "on," for a total presentation duration of 144 s. Each of these "trials" was then repeated with and without optogenetic stimulation, alternating conditions every trial and acquiring between eight and 40 trials per cell or network.

Natural movies ($n = 3$) were selected from the van Hateren natural movie database. Gray-scale values of each movie were discretized to 255 values, and each frame was normalized to have equal mean luminance (mean of histogram = 128) and contrast (SD = 32). To slow down the movie from its original 60-Hz frame rate, we updated every three frames, creating an effective frame rate of close to 20 Hz. Movies were presented for 4 s and were flanked by 2-s gray screens (mean luminance = 128). Each movie was repeated 10 times to calculate response reliability.

Systemic Administration of rhIGF1 and Bumetanide. Animals were weighed and injected i.p. once daily with either vehicle (saline) or rhIGF1 (2.5 mg/kg; Peprotech) dissolved in saline with 0.01% BSA (wt/vol). Animals were kept in individual home cages and injected daily for 10–14 d, starting on P30 (for gKO) or P45 (for cKO) as described earlier (28). For chloride cotransporter experiments, animals were injected with rhIGF1 for 7–10 d starting at P14. Bumetanide (B3023-1G; Sigma) was injected i.p. (0.2 mg/kg) once daily for 3–4 d, starting at P10. The injection solution was made in 2% DMSO dissolved in saline.

Immunohistochemistry. Immediately after physiology experiments, mice were overdosed with isoflurane and transcardially perfused with saline, followed by 4% PFA. The brain was extracted and placed in 1× PBS, and 40-μm sections were then cut with a vibratome. Sections were treated with 1% sodium borohydride in PBS for 10 min to cleave aldehyde fixation and improve signal for SOM, blocked in 10% goat serum and 0.1% Triton in PBS for 120 min at room temperature on a shaker, and incubated overnight at 4 °C in primary antibody for SOM (rabbit anti-SOM, 1:200, AB5494; Millipore), Pv (mouse anti-Pv, 1:250, MAB1572, Chemicon; rabbit anti-Pv, 1:500, PV27, Swant), MeCP2 primary antibody (mouse anti-MeCP2, 1:500, M7443; Sigma), IGF1 receptor (mouse anti-IGF1R, 1:500, ab54274; Abcam), Otx2 (rabbit anti-Otx2, 1:1,000, AB9566; Millipore), and perineuronal nets biotinylated Wisteria floribunda agglutinin (WFA), 10 μg/mL, B1355; Vector Labs]. Sections were then washed three times and incubated in secondary antibody for either SOM (biotinylated goat anti-rabbit; Vector Labs) or Pv (goat anti-guinea pig Alexa Fluor 488, 1:200, A11073; Molecular Probes). The SOM staining was amplified with Streptavidin-FITC (Molecular Probes). Sections were mounted on slides and coverslipped with Vectashield Hardset mounting media with DAPI (Vector Labs). Images of immunofluorescent sections were taken at a magnification of 20× with a confocal microscope (LSM5 Exciter; Zeiss) and quantified with ImageJ software (NIH). Cell counts and overlap were quantified using ImageJ software.

Western Blot. Protein samples were collected from dissected mouse brain V1 tissue with radioimmunoassay lysis buffer [150 mM NaCl, 25 mM Tris·HCl, 1 mM EDTA, 1% Nonidet P-40, 1% Sodium Deoxycholate, 0.1% SDS, with protein kinase inhibitor and protease inhibitor (pH adjusted to 7.6)]. A sonication step was applied to homogenize tissue and extract protein, followed by a 10- min centrifugation at 4 °C. The protein samples were mixed with NuPAGE LDS sample buffer, heated at 95 °C for 10 min, and then separated on NuPAGE 4–12% Bis-Tris gel and transferred to PVDF membrane. The PVDF membrane was blocked for 30 min with 5% milk in TBS + 0.1% Tween 20 (TBST), and incubated overnight at 4 °C with primary antibodies diluted in TBST and milk at the following concentrations: KCC2 (1:2,000; Millipore), NKCC1 (1:1,000; Iowa Hybridoma bank), α-tubulin (1:4,000; Abcam), and GAPDH (1:3,000; Abcam). The membrane was rinsed with TBST three times to wash off excess antibodies, and then incubated in secondary HRP antibodies in TBST and milk at a 1:5,000 concentration. The chemiluminescence method (HRP substrate; Millipore) detected clear KCC2 protein monomer (∼120 kDa) and dimer (>200 kDa) bands. The PVDF membrane was then stripped using Reblot Plus Strong Antibody Stripping Solution (Millipore), and reimmunoblotted for NKCC1 (∼150 kDa) to acquire the KCC2/NKCC1 ratio. The area and intensity of protein signal were determined using ImageJ. Relative KCC2 and NKCC1 expression was calculated by normalizing protein signal to GAPDH or a tubulin loading control. We detected both monomeric and dimeric KCC2 bands in P20 WT and gKO mouse brain, and combined them together while quantifying KCC2 expression. KCC2 expression during early development (P8) remains low, and the KCC2 dimer band is faint. Hence, we only quantified the monomer band.

Data Analysis. Data were acquired directly into MATLAB via custom software (Network Prism, M.S. laboratory) and saved as .mat files. Spike detection was performed via analysis routines that used manually defined thresholds, followed by spike shape template matching for further verification. Every spike was tagged and displayed on the screen in a graphical user interface, whereupon it was manually reviewed for false-positive and negative results by an experimenter. Spike times in response to every stimulus were then grouped into "on" or "off" periods based on their timing relative to visual stimulation, and on-spikes for each stimulus were decremented by the number of off-spikes observed during an equal time period. For orientation experiments, the number (#) of spikes per stimulus = (# spikes on) − (# spikes off) because on- and off-periods were of the same duration.

For calcium imaging experiments, we used a temporal deconvolution algorithm (41) to estimate neural firing rates from the recorded calcium transients. Visually responsive cells were determined by performing a one-tailed Student's t test between visually evoked responses (4-s stimulus) and spontaneous responses (4-s gray screen). Only cells with $P < 0.001$ were classified as visually responsive.

Cells were selected for analysis based on Gaussian fits to their responses, and analyzed using the OSI. Gaussian fits were computed for the tuning curves using a sum of two Gaussians (cell data) with peaks 180° apart and five parameters: preferred orientation, θp; tuning width, σ (shared by the two directions); baseline response, $R0$; response at the preferred orientation, Rp; and response at the null orientation, Rn. Optimal parameters were determined with least-squares fits using MATLAB's *lsqnonlin* routine. Goodness of fit was determined from the R^2 value $\{R^2 = 1 - [\sum_i (y - f)^2]/[\sum_i (y - \hat{y})^2]\}$. Only cells with $R^2 > 65\%$ and

with significant visually evoked responses ($P < 0.001$) were selected for further analysis. The peak response was taken to be the maximum response at the preferred orientation. For quantitative analyses, the OSI was computed by taking the vector average of responses to all orientations, according to the formula:

$$\mathrm{OSI} = \frac{\sqrt{\left(\sum_i R(\theta_i)\sin(2\theta_i)\right)^2 + \left(\sum_i R(\theta_i)\cos(2\theta_i)\right)^2}}{\sum_i R(\theta_i)}.$$

Reliability and Sparseness Analysis. Lifetime sparseness provides a measure of the selectivity of a neural response to a visual scene. Cells with a sparseness of 0 imply dense and unselective responses, whereas cells with a sparseness of 1 selectively encode only one feature (41). Sparseness was calculated using the equation shown below, where R_i is the response to the ith movie frame (averaged over trials) and N is the number of frames:

$$\mathrm{Sparseness} = \frac{N - \frac{\left(\sum_i R_i\right)^2}{\sum_i R_i^2}}{N-1}.$$

Response reliability measures spiking precision between trials. A highly reliable neuron responds with stereotypical responses on each repetition of the stimulus. As a result, a highly reliable neuron would have a between-trial Pearson's correlation coefficient of 1:

$$\mathrm{Reliability} = \frac{2}{T^2 - T}\sum_{i=1}^{T}\sum_{j=1+1}^{T}\rho(R_i, R_j).$$

Following the equation above, reliability was calculated as the average Pearson's correlation of all pairwise combinations of trials (T) for a single movie. Only neurons with significant responses on more than 10 trials were selected for this analysis.

Statistical Analysis. All statistical analysis was performed using custom-written routines in MATLAB. The Shapiro–Wilk test was first used to determine if the data were normally distributed. Nonparametric one-way ANOVA (Kruskal–Wallis test) was performed to determine statistical significance between experimental conditions. Further comparisons were made relative to WT data using Bonferroni-corrected rank-sum tests.

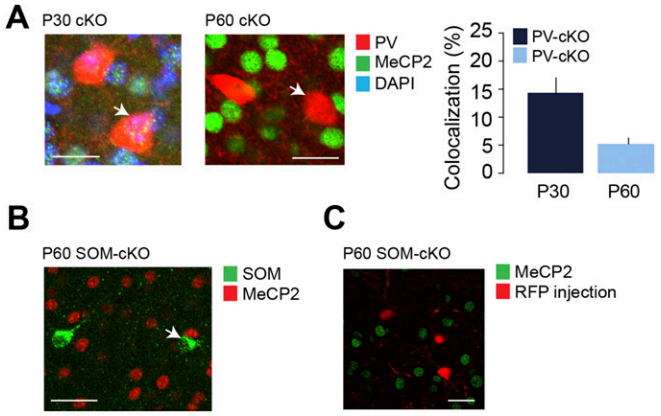

Fig. S1. Interneuron-specific deletion of MeCP2. (*A*) Immunostaining showing interneuron subtype-specific deletion of MeCP2 in PV-cKO mice. The PV^+ locus is turned on late during postnatal development, and we confirmed that Cre-dependent MeCP2 deletion was complete around P60. White arrows show MeCP2 staining (in green) in PV^+ neurons (in red) in P30 PV-cKO mice, which is absent at P60. (Scale bar: 20 μm.) (*B*) Immunostaining showing SOM^+ neuron-specific MeCP2 deletion in P60 SOM-cKO mice. The white arrow shows the absence of MeCP2 staining (in red) in SOM^+ neurons (in green). (Scale bar: 50 μm.) (*C*) SOM^+ cells specifically labeled with lox-STOP-lox (LSL)-RFP in a cKO mouse. Immunostaining showing MeCP2 (in green) is absent in these RFP^+ neurons (Scale bar: 20 μm.).

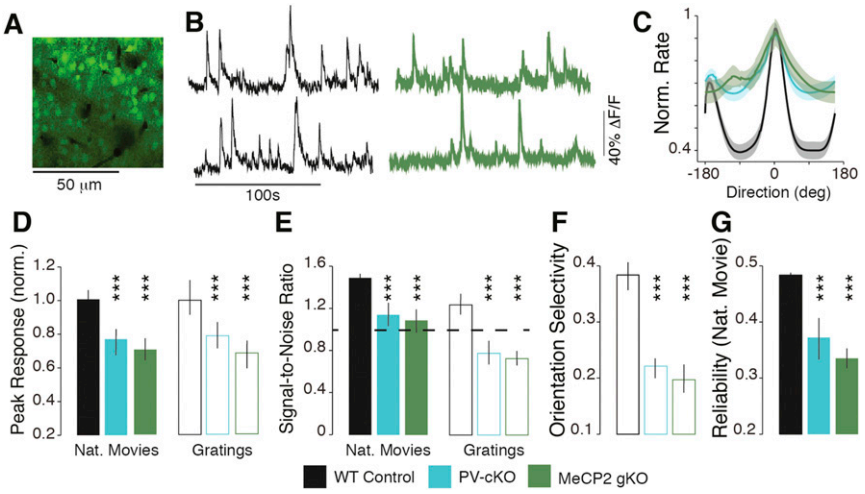

Fig. S2. Comparison of the response properties of pyramidal neurons in awake, head-fixed mice. (*A*) Example population of neurons labeled with OGB-1. (*B*) Example calcium transients from two neurons from a WT control animal (*Left*) and two neurons from an MeCP2 gKO animal (*Right*). ΔF/F, changes in fluorescence activity. (*C*) Population-averaged tuning curves from WT ($n = 53$ neurons in three mice), PV-cKO ($n = 25$ neurons in two mice), and MeCP2 gKO ($n = 28$ neurons in two mice) conditions. These tuning curves were centered at 180°; the shaded area represents SEM. deg, degrees. (*D*) Quantification of normalized firing rate in response to natural movies (filled bars) and gratings (open bars) from WT ($n = 156$ neurons), PV-cKO ($n = 79$ neurons), and MeCP2 gKO ($n = 99$ neurons) conditions. (*E*) Quantification of signal-to-noise ratio for both natural movies and gratings. (*F*) Quantification of mean orientation selectivity measured from drifting gratings. (*G*) Quantification of mean reliability measured from natural movies. All data in *D*–*G* are represented as mean ± SEM. ***$P <$ 0.0001, Kruskal–Wallis ANOVA with Bonferroni correction with post hoc rank-sum tests relative to WT. Nat., natural; norm., normalized.

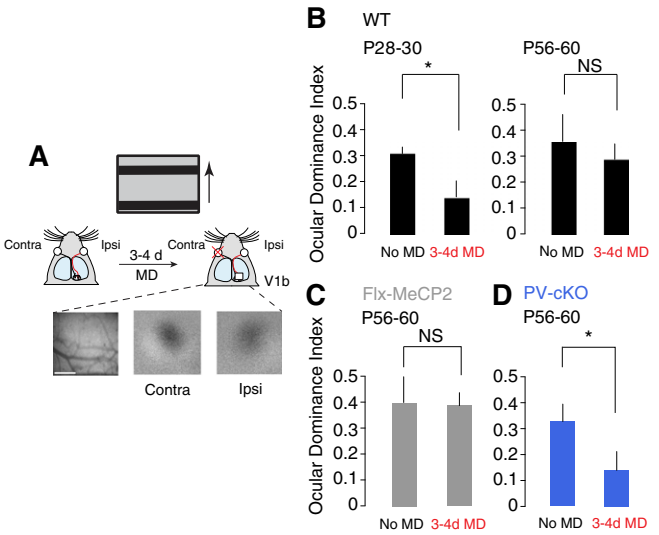

Fig. S3. Visual cortex plasticity induced by MD extends into adulthood after MeCP2 deletion. (*A*) Eye-specific responses recorded from binocular V1 (V1b) using optical imaging of intrinsic signals after a 3- to 4-d MD. (*Bottom*) Blood vessel image and representative response maps showing contralateral (Contra) and ipsilateral (Ipsi) eye responses in V1 of a WT mouse (Scale bar: 200 μm.) (*B*) WT male mice (no MD, $n = 3$) show normal plasticity during the critical period (P28–30), where an OD shift is seen after 3–4 d of contralateral eye deprivation (MD, $n = 4$ mice). Plasticity is absent after similar deprivation in adulthood (P56–60; no MD, $n = 4$ mice; MD, $n = 4$ mice). (*C*) Flox-MeCP2 animals also show no change in ODI at P56–60 (no MD, $n = 4$ mice; MD, $n = 5$ mice). (*D*) Adult (P56–60) PV-cKO animals show an OD shift (no MD, $n = 4$ mice; MD, $n = 5$ mice). All values are expressed as mean ± SEM. *$P < 0.05$, Wilcoxon rank-sum test treating each animal as an individual observation. NS, not significant.

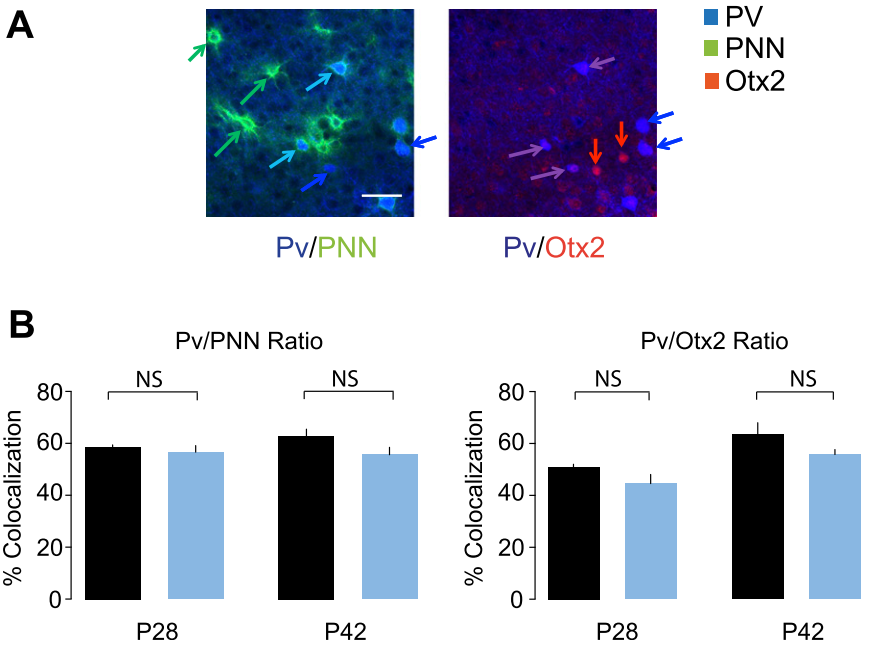

Fig. S4. Normal expression of PV$^+$ structural and maturational markers in MeCP2 gKO mice. (*A*) Coimmunostaining against PV$^+$ (PV) and perineuronal nets (PNN; *Left*) and homeodomain protein Otx2 (*Right*) in V1 of a P28 WT mouse. (Scale bar: 25 μm.) (*B*) Colocalization of PV and PNN (*Left*) and PV and Otx2 (*Right*) is not significantly different in MeCP2 gKO mice (blue) compared with their WT littermates (black bars) at P28 or P42 ($n = 3$ mice for each condition) NS, $P > 0.05$ (Student's *t* test). All values are mean ± SEM.

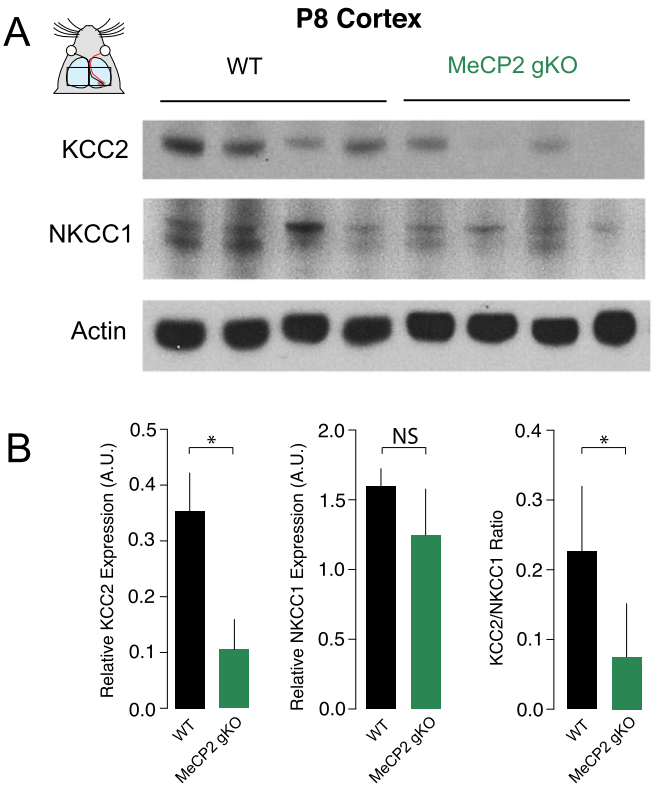

Fig. S5. Reduced KCC2 expression and KCC2/NKCC1 ratio in P8 MeCP2 gKO mice. (*A*) Western blot measurements using cortical homogenates showing expression profile of NKCC1 and KCC2. (*B*) Relative KCC2 expression (normalized to actin loading control) and KCC2/NKCC1 ratio are reduced in the cortex of P8 MeCP2 gKO mice compared with their age-matched WT littermate controls (WT, $n = 4$ mice; MeCP2 gKO, $n = 4$ mice). $^*P < 0.05$, Student's t test. No difference in relative NKCC1 expression was observed between the two genotypes (NS, $P > 0.05$). All values are mean ± SEM. A.U., arbitrary units.

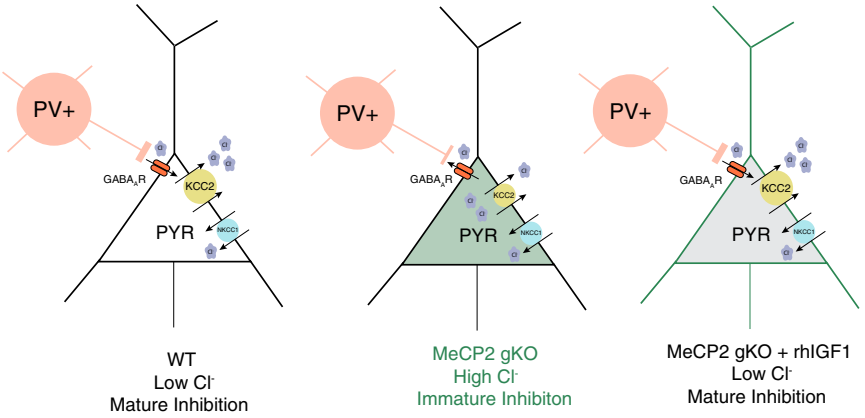

Fig. S6. rhIGF1 reverses defective GABAergic polarity in MeCP2 gKO mice. Cartoon showing defective Cl^- signaling due to reduced expression of KCC2 in MeCP2 gKO mice (green filled), leading to immature inhibition via depolarizing GABAergic transmission. rhIGF1 treatment (green border) increases the expression of KCC2, restoring the Cl^- balance and hyperpolarizing nature of inhibition. PYR, pyramidal cells.